Bioactive Materials 6 (2021) 386–403

Contents lists available at ScienceDirect

Bioactive Materials

journal homepage: http://www.keaipublishing.com/biomat

Bistratal Au@Bi_2S_3 nanobones for excellent NIR-triggered/multimodal imaging-guided synergistic therapy for liver cancer

Ruizhuo Ouyang[a,*,1], Penghui Cao[a,1], Pengpeng Jia[a,1], Hui Wang[a,1], Tianyu Zong[a], Chenyu Dai[a], Jie Yuan[a], Yuhao Li[a], Dong Sun[c], Ning Guo[a], Yuqing Miao[a,*], Shuang Zhou[b]

[a] Institute of Bismuth Science, University of Shanghai for Science and Technology, Shanghai, 200093, China
[b] Cancer Institute, Tongji University School of Medicine, Shanghai, 200092, China
[c] School of Chemistry and Chemical Engineering, Henan Normal University, Xinxiang, 453007, China

ARTICLE INFO

Keywords:
Au@Bi_2S_3 NBs
DOX
CT
Photothermal conversion
Cancer treatment

ABSTRACT

To fabricate a highly biocompatible nanoplatform enabling synergistic therapy and real-time imaging, novel Au@Bi_2S_3 core shell nanobones (NBs) (Au@Bi_2S_3 NBs) with Au nanorods as cores were synthesized. The combination of Au nanorods with Bi_2S_3 film made the Au@Bi_2S_3 NBs exhibit ultrahigh photothermal (PT) conversion efficiency, remarkable photoacoustic (PA) imaging and high computed tomography (CT) performance; these Au@Bi_2S_3 NBs thus are a promising nanotheranostic agent for PT/PA/CT imaging. Subsequently, poly(N-vinylpyrrolidone)-modified Au@Bi_2S_3 NBs (Au@Bi_2S_3-PVP NBs) were successfully loaded with the anticancer drug doxorubicin (DOX), and a satisfactory pH sensitive release profile was achieved, thus revealing the great potential of Au@Bi_2S_3-PVP NBs in chemotherapy as a drug carrier to deliver DOX into cancer cells. Both *in vitro* and *in vivo* investigations demonstrated that the Au@Bi_2S_3-PVP NBs possessed multiple desired features for cancer therapy, including extremely low toxicity, good biocompatibility, high drug loading ability, precise tumor targeting and effective accumulation. Highly efficient ablation of the human liver cancer cell HepG2 was achieved through Au@Bi_2S_3-PVP NB-mediated photothermal therapy (PTT). As both a contrast enhancement probe and therapeutic agent, Au@Bi_2S_3-PVP NBs provided outstanding NIR-triggered multi-modal PT/PA/CT imaging-guided PTT and effectively inhibited the growth of HepG2 liver cancer cells *via* synergistic chemo/PT therapy.

1. Introduction

Cancer is widely regarded as the leading cause of death and is mostly identified at an advanced stage, when surgery is no longer the first choice to resect tumors, and only a few traditional treatment regimens, such as chemotherapy, are available [1]. Cancer patients usually experience severe side effects and drug resistance from conventional chemotherapy, owing to the poor solubility and non-targeting properties of drugs [2,3]. To overcome these issues, many efforts have been made to design biocompatible nanomaterials to deliver conventional chemotherapy drugs to tumor sites and achieve a synergistic therapeutic effect under pH/photothermal (PT) sensitive profiles [1,2,4], [5]. Exploring simple methods to prepare core-shell structured nanocomposites as drug carriers and PT conversion agents is of great importance and has attracted much attention as a means to potentially achieve diagnostic and therapeutic functions simultaneously [3,6–8]. Because of the high absorption efficiency and photothermal conversion efficiency (PCE, η) in the near-infrared (NIR) region, gold nanorods (Au NRs) are preferred and promising candidates for broad biomedical applications such as photothermal therapy (PTT), photodynamic therapy, photoacoustic (PA) imaging, surface enhanced Raman spectroscopy and labels in diagnostics and sensors [9–17]. Because Au NRs exhibit low photostability owing to the melting effect, and easily cluster and aggregate, thereby restricting their applications in PTT [18], the surfaces of Au NR-based nanoplatforms are usually modified with different materials including inorganic materials [6,19], polymers [14,18]

Peer review under responsibility of KeAi Communications Co., Ltd.
* Corresponding authors.
E-mail addresses: ouyangrz@usst.edu.cn (R. Ouyang), cph806259@163.com (P. Cao), ppjia2020@sinano.ac.cn (P. Jia), wh18567606282@163.com (H. Wang), tianyuzong@outlook.com (T. Zong), 18070290218@163.com (C. Dai), yuanj@sphchina.com (J. Yuan), yhli@usst.edu.cn (Y. Li), sundong2004@htu.edu.cn (D. Sun), guoning@usst.edu.cn (N. Guo), yqmiao@usst.edu.cn (Y. Miao), shuangzhou@tongji.edu.cn (S. Zhou).
[1] R. Ouyang, P. Cao, P. Jia and H. Wang contributed equally to this work.

https://doi.org/10.1016/j.bioactmat.2020.08.023
Received 19 May 2020; Received in revised form 17 August 2020; Accepted 26 August 2020

and metal-organic frameworks (MOFs) [13,20,21], thereby forming hybridized nanocomposites that exploit the excellent optical performance of Au NRs. For instance, Bao and coworkers have synthesized dumbbell-like Au NR-Cu_7S_4 core-shell heterostructures that significantly increase the η to 62%—much higher than that of single Au NRs (η = 39%) [19]. Wang et al. have combined a polyaniline derivative poly (o-methoxyaniline) (POMA) with Au NRs to form POMA/Au NR core-shell hybrids with high PCE (η = 21.8%) [14]. Porphyrinic MOFs have also been used with individual Au NRs incorporated inside, thus producing delicate core-shell composites with enhanced drug loading efficiency, NIR light-triggered drug release capability and a PCE of 20.6%. After the surface modification of Au NRs, both clustering and aggregation can be effectively inhibited. However, polymers or MOFs can be typically separated from Au NRs and not even be excreted easily from the body, thus prompting concerns about their stability and potential toxicity. Moreover, the PCE is relatively low [15].

Among all the transition metals, bismuth, a biocompatible metallic element, remarkably has nonexistent toxicity and excellent tolerance even with large doses [22]. It is worth mentioning that the PT properties of bismuth are better than those of the reported copper PT agents, such as Au NR-Cu_7S_4, that produce long-term toxicity due to the metal ions. The commercialization of bismuth-relevant drugs has spread worldwide, owing to the good results in treating several diseases, typically gastropathy infected by *Helicobacter pylori* [23–28]. Because of the high atomic number (Z = 83) of bismuth, Bi_2S_3 has been used as a theranostic nanomedicine for precise cancer diagnostics with the assistance of computed tomography (CT) imaging. These applications are facilitated by these nanomaterials' outstanding properties including X-ray attenuation capability (Bi, 5.74 cm^2/g at 100 keV; I, 1.94 cm^2/g at 100 keV; Au, 5.16 cm^2/gat 100 keV; Pt, 4.99 cm^2/g at 100 keV), long residence time, low toxicity, ease of metabolism as well as NIR light-induced PTT performance [29–33], which decreases the required dose and enables more flexibility in clinical settings. Recently, considering the good PT performance of Au and Bi_2S_3, Zhang and coworkers synthesized Bi_2S_3–Au NRs by incorporating Au NPs into Bi_2S_3 NRs. The PT performance of Bi_2S_3 NRs has been found to be significantly enhanced under NIR laser irradiation [32], with an ultrahigh PCE of 51.06%, owing to the enhancement of nonradiative electron-hole recombination inside Bi_2S_3 NRs in the presence of Au NPs. The Bi_2S_3–Au NRs were easily internalized by cancer cells and subsequently caused more severe cell apoptosis and effective inhibition of tumor growth than single Bi_2S_3 NRs under irradiation by a 808 nm NIR laser, thus exhibiting great potential for CT imaging-guided PTT for cancer.

Here, we asked how the PT performance of Au NRs might be affected if Bi_2S_3 were combined with Au NRs to form Au@Bi_2S_3 NPs. *Via* a simple method, we thus synthesized Au@Bi_2S_3 nanobones (Au@Bi_2S_3 NBs) as a potential theranostic nanoplatform, which was applied to enable the first described NIR-triggered PTT. Scheme 1 illustrates the fabrication of Au@Bi_2S_3 NBs as the theranostic agent in synergistic cancer therapy. First, Au NRs was synthesized according to a previously reported method [34]. L-ascorbic acid (AA), hexamethylenetetramine and thioacetamide (TAA) were then thoroughly mixed with Au NR-containing solution to synthesize Au@Bi_2S_3 NBs with subsequent addition of bismuth acetate. Under vacuum, the mixture stood for 8 h at 80 °C to form the Au@Bi_2S_3 core-shell NBs. Second, poly(vinylpyrrolidone) (PVP) was used to functionalize the Au@Bi_2S_3 NBs (Au@Bi_2S_3-PVP NBs) to increase the biocompatibility, prolong the residence time *in vivo* and improve the loading performance toward doxorubicin (DOX). Third, the precise visualization of trace Au@Bi_2S_3-PVP NBs accumulating in the tumors was performed through PT ablation and PA/CT imaging. The multiple functions of Au@Bi_2S_3-PVP NBs as an effective contrast agent in angiography and an efficient PT agent allowed for excellent real-time monitoring and efficient treatment of tumors. Finally, Au@Bi_2S_3-PVP NBs were efficiently internalized into HepG2 human liver cancer cells and induced severe cell injury upon NIR laser irradiation. After subcutaneous administration to female BALB/c tumor-bearing nude mice, the tumor sites were easily visualized as Au@Bi_2S_3-PVP NBs accumulated inside tumors, owing to their outstanding PA/CT imaging ability and PT effects. After treatment, tumor growth was effectively inhibited without affecting the body weight of mice, and no obvious pathological changes were found in major organs, a result indicative of the low toxicity and expected biocompatibility of these NBs. Therefore, the new and feasible method described here enabled fabrication of an effective theranostic nanoplatform with a powerful multimodal imaging-guided chemo/PT capacity for precise cancer treatment.

2. Materials & methods

2.1. Chemicals and reagents

Cetyl trimethyl ammonium bromide (CTAB, > 98.0%), tetraethylorthosilicate (TEOS, GR), 5-bromosalicylicacid (> 98.0%), hydrogen tetrachloroaurate trihydrate ($HAuCl_4{\cdot}3H_2O$), silver nitrate ($AgNO_3$, > 99%), sodium borohydride ($NaBH_4$, 99%), bismuth acetate (99.5%), bismuth nitrate pentahydrate ($Bi(NO_3)_3{\cdot}5H_2O$), sodium sulfide nonahydrate ($Na_2S{\cdot}9H_2O$), sodium hydroxide (NaOH, 96%), AA, hexamethylenetetramine, DOX, PVP, TAA and 4′,6-diamidino-2-phenylindole (DAPI) were purchased from J&K Scientific Ltd. (Shanghai, China) and used without further purification. 3-(4, 5)-dimethylthiahiazo-2-yl)-2,5-diphenyltetrazolium bromide (MTT) was obtained from Sigma (cat. M2003). Fresh doubly distilled water was used to make all aqueous solutions. All relevant glassware was immersed in aqua regia and thoroughly washed with doubly distilled water, then dried in an air dry oven.

2.2. Characterization

The morphology, size and structure of the synthesized core-shell Au@Bi_2S_3 NBs were determined through transmission electron microscopy (TEM, Tecnai G2 F20 S-Tcin). UV–Vis absorbance was recorded on a UV–Vis 1901 spectrophotometer (Phoenix). X-ray photoelectron spectroscopy (XPS) was performed on an ESCALAB 250Xi (Thermal Scientific). Contact angles of materials were measured through DataPhysics OCA-Series. A Flir E40 compact infrared thermal imaging camera (FLIR Systems, U.S.A) was used to measure the thermographs. The *in vivo* imaging was performed with a NightOWL II LB983 instrument (Berthold, Germany).

2.3. Preparation of Au NRs and core-shell Au@Bi_2S_3 NBs

Preparation of Au NRs: The Au NRs were produced using the previously reported seed-growing method [34]. First, 0.364 g CTAB was dissolved in 9.75 mL H_2O, and this was followed by the addition of 250 μL 10 mM $HAuCl_4$. Second, 1.0 mL 60 mM $NaBH_4$ aqueous solution was thoroughly mixed with the above yellow solution under rapid stirring, and the color quickly changed to brown. After 2 min of stirring, the seed solution was obtained and kept stationary at 30 °C for 30 min for subsequent use. Third, 23.80 mL doubly distilled water containing 0.45 g CTAB and 55 mg 5-bromosalicylic acid was heated in a 50 mL Erlenmeyer flask while stirring until both CTAB and 5-bromosalicylic acid were completely dissolved. Then, 0.60 mL 40 mM $AgNO_3$ solution was added dropwise after the temperature of the solution decreased to 30 °C. After 30 min, 1.25 mL 10 mM $HAuCl_4$ solution was subsequently added under slow stirring (~400 rpm). The stirring continued for 15 min. Afterward, 64 μL 0.1 M AA was pipetted in, and the resulting solution was vigorously stirred for 30 s, thus forming a colorless growth solution. Immediately, 40 μL seed-containing solution was accurately transferred into the above prepared solution of growth with stirring for 30 s and was kept undisturbed overnight (about 12 h) at 30 °C to allow the growth of bone-like Au NRs (Au NBs). Finally, the Au NBs were obtained after centrifugation at 18,000 rpm for 15 min, followed by two

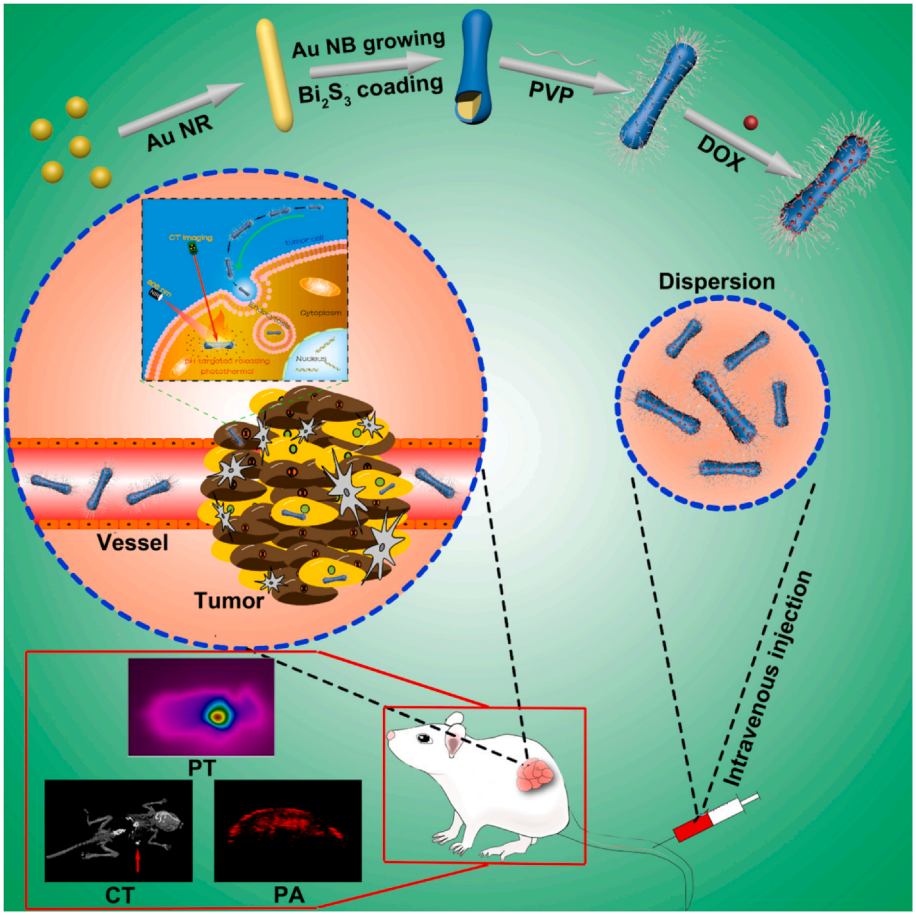

Scheme 1. The scheme of the DOX loaded Au@Bi_2S_3-PVP NBs for PT/PA/CT imaging and chemo/PT synergetic therapy for liver cancer.

washes with water and redispersion in 20 mL water.

Preparation of core-shell Au@Bi_2S_3 NBs: For synthesis of Au@Bi_2S_3 NBs, 5.0 mL uncentrifuged Au NB solution was first placed in a round-bottom flask (25 mL), and 1.0 mL 0.1 M AA, 1.0 mL 0.1 M hexamethylenetetramine and 0.04 mL 0.1 M thioacetamide were then successively pipetted in. After the color changed from magenta to deep purple, 0.01 mL of 0.1 M bismuth acetate was added. Under vacuum, the obtained mixture was stored without being disturbed for 8 h at 80 °C to allow formation of the Au@Bi_2S_3 core-shell NBs. Afterward, the prepared Au@Bi_2S_3 NBs were collected by centrifugation of the mixture containing Au@Bi_2S_3 NBs at 18,000 rpm for 15 min and were subsequently washed with water. Then 3.0 mL of Au@Bi_2S_3 NB solution was mixed with 5.0 mL doubly distilled water containing 4.0 mg PVP for reaction. The solution was sonicated for 20 min and stirred for 30 min. The finally collected Au@Bi_2S_3-PVP NBs were stored in deionized water for subsequent use.

2.4. Surface plasmon enhancement

Preparation of Bi_2S_3 NRs: The Bi_2S_3 NRs were synthesized with an environmentally friendly solvothermal method. Briefly, 0.249 g Bi$(NO_3)_3{\cdot}5H_2O$ was first mixed with 35 mL ethylene glycol solution under vigorous stirring. After 30 min of stirring, 1.0 mL aqueous solution containing 0.18 g $Na_2S{\cdot}9H_2O$ was slowly added to the mixed solution, which was vigorously stirred for 2 min and became black. The mixture was then transferred into a 50 mL Teflon-lined autoclave and heated at 180 °C for 2 h in an electric blast drying oven after being completely sealed. After the autoclave naturally cooled to room temperature, the nano-products were collected by centrifugation and successively washed two times with ethanol and doubly distilled water to remove the excess impurities.

UV–Vis measurements: The UV–vis spectra of 100 μg mL^{-1} Au NRs, 100 μg mL^{-1} Bi_2S_3 NRs, 100 μg mL^{-1} Au NRs mixed with 100 μg mL^{-1} Bi_2S_3 NRs, and 100 μg mL^{-1} Au@Bi_2S_3 NBs were obtained with a UV–Vis 1901 spectrophotometer (Phoenix).

2.5. Physiological stability of Au@Bi_2S_3-PVP NBs

The freshly prepared Au@Bi_2S_3 NBs were dispersed in doubly distilled water, PBS (pH 7.4) and Dulbecco's modified Eagle's medium (DMEM, containing 10% fetal bovine serum (FBS) and 1% penicillin streptomycin (PS)) with a solution concentration of 25 μg mL^{-1}. The hydrated particle size distributions (HD) of Au@Bi_2S_3 NBs in three solutions were measured daily within the first 7 days.

2.6. In vitro drug loading and release

Twelve milligrams of as-prepared Au@Bi_2S_3 core-shell NBs was added into 30 mL PBS (pH 7.4) containing 3.0 mg DOX. After being completely mixed under stirring at room temperature, the mixed solution was stored in the dark for 48 h to obtain the final stable DOX-loaded Au@Bi_2S_3-PVP NB solution. The obtained mixture was washed twice with PBS to remove the weakly bonded or free DOX immediately after 10-min centrifugation at 12,000 rpm. At 483 nm, the UV–Vis absorbance value of the supernatant was subsequently measured. On the basis of equations (1) and (2) below, the encapsulation efficiency and loading content of DOX that physically adsorbed on the surfaces of Au@Bi_2S_3-PVP NBs were calculated:

Encapsulation efficiency = DOX weight in Au@Bi_2S_3-PVP NBs/total

weight of used DOX (1)

Loading content = DOX weight in Au@Bi_2S_3-PVP/weight of Au@Bi_2S_3-PVP/DOX NBs (2)

In the *in vitro* drug release experiment, 5.0 mL PBS (pH 7.4) and 5.0 mL HAc/NaAc buffer (pH 5.0) were used to disperse the as-prepared Au@Bi_2S_3-PVP/DOX nanocomposites under stirring and ultrasonication, respectively, thus forming two 1.0 mg mL^{-1} Au@Bi_2S_3-PVP/DOX solutions as release media. The UV–Vis absorbance value of the released DOX was measured at 483 nm every 1 h according to the following protocol. Briefly, the release medium was stirred at 37 °C and centrifuged at 12,000 rpm for 10 min. A certain volume of supernatant was then acquired and measured with the same volume of the corresponding release medium supplemented subsequently.

2.7. Evaluation of PT performance

To evaluate the PT properties of Au@Bi_2S_3 NBs, we placed 1.0 mL of Au@Bi_2S_3 NB aqueous solutions at concentrations of 0, 6.25, 12.5, 25, 50 and 100 ppm in a 48-well culture plate which was irradiated with an 808 nm laser for 5 min. The power density ranged from 0 to 3.4 W/cm^2. During irradiation of the Au@Bi_2S_3 NB solutions, a thermocouple probe was placed perpendicular to the laser path to avoid the direct irradiation of light on the probe. The temperature of the Au@Bi_2S_3 NB solutions was recorded every 30 s by a digital thermometer with a 10 mm diameter laser module.

2.8. Hemolysis assay

Healthy human blood samples were provided by the Department Laboratory Diagnostics of Changhai Hospital (Shanghai, China) and approved for research purposes by the China Committee for Research and Animal Ethics. After the addition of 10 mL PBS to a 5.0 mL blood sample, the mixture was fully mixed, and this was followed by a 10-min centrifugation at 3000 rpm. After removal of the supernatant, the remaining red blood cells (RBCs) were washed five times with PBS and redispersed in 50 mL PBS. Both positive and negative controls were set with distilled water and PBS, respectively. An 0.8 mL volume of Au@Bi_2S_3-PVP PBS solution at different concentrations was then individually mixed with 0.2 mL diluted RBCs and allowed to stand undisturbed for 4 h at room temperature. Immediately before the UV–Vis absorbance measurement at 570 nm, each solution was centrifuged for 10 min (12,000 rpm). Equation (3) below was used to calculate the hemolysis ratio induced by Au@Bi_2S_3-PVP NBs [35,36]:

Hemolysis ratio = {(absorbance value per group - absorbance value in the control (−) group)/(absorbance value in the control (+) group - absorbance value in the control (−) group)} × 100% (3)

2.9. Culture of HepG2 cells

The culture of HepG2 human liver cancer cells was performed in DMEM (high glucose, penicillin: 80 U/mL, streptomycin: 0.08 mg mL^{-1}, Keygenbio) containing 10% FBS. The cultivation environment was 5% CO_2 and 37 °C.

2.10. In vitro cytotoxicity of Au@Bi_2S_3-PVP NBs

In a 96-well plate, HepG2 cells were seeded at a density of 1×10^4 cells/well for 12 h and allowed to attach to the bottom. The cells were incubated in complete Au@Bi_2S_3-PVP NB-containing medium at different concentrations (1, 5, 10, 25, 50, 100, 150 and 300 μg mL^{-1}) for 24 h at 37 °C with 5% CO_2. Afterward, 10 μL of 5.0 mg mL^{-1} MTT solution was added in each well and incubated for another 4 h. After removal of the culture medium, 100 μL DMSO was added into each well. The 96-well plate was subsequently shaken for 10 min on a shaker to fully dissolve the purple crystals at the bottom of the wells. Finally, the measurement of UV–Vis absorbance of formazan in each well was completed at 570 nm with a plate reader. In each group, five parallel measurements were collected.

2.11. Cell uptake of Au@Bi_2S_3-PVP/DOX NBs

HepG2 cells were first seeded in 12-well plates at a density of 2×10^5 cells/well. Then, the medium was removed after all cells adhered to the well bottoms. Subsequently, cells were incubated for 2 h with 20 μg mL^{-1} DOX and 100 μg mL^{-1} Au@Bi_2S_3-PVP/DOX, respectively. After the medium was removed through gentle rinsing of the adherent cells, the cells were stained with DAPI and observed under an inverted fluorescence microscope.

2.12. In vitro inhibition of free DOX, Au@Bi_2S_3-PVP NBs and Au@Bi_2S_3-PVP/DOX NBs

A 96-well plate was used to seed HepG2 cells at a density of 1×10^4 cells/well and placed in a cell incubator for 12 h to allow attachment to the well bottom. The cells were then incubated for 4 h in complete medium containing DOX, Au@Bi_2S_3-PVP NBs and Au@Bi_2S_3-PVP/DOX NBs at equivalent concentrations. PBS was used to rinse the wells three times to remove excess free inhibitors. For the PT and PT-chemotherapy treatment, each well was irradiated for 3 min with an 808 nm laser. The output power density was 1.45 W/cm^2. Afterward, another 24 h incubation was performed. Finally, the cell viability in each well was investigated *via* the MTT method. Five parallel measurements were collected for each group.

2.13. In vitro fluorescence staining of different treatments

HepG2 cells were seeded in 12-well plates with a cell density 2×10^5 cells/well and placed in a cell incubator for 24 h to allow cells to adhere to the well bottoms. Then the treatments were separately conducted with Au@Bi_2S_3-PVP, DOX, Au@Bi_2S_3-PVP/DOX, Au@Bi_2S_3-PVP + NIR and Au@Bi_2S_3-PVP/DOX + NIR. After the 24 h incubation, the unattached NBs were removed through gentle rinsing of the adherent cells. Fresh medium was then added. An 808 nm laser was chosen to irradiate the differently treated cells in each well for 3 min at an output power density of 1.45 W/cm^2, and propidium iodide (PI) was used to stain the cells (red nuclear stain). After laser irradiation, the combined therapy (PT and chemotherapeutic effects) of cells was monitored during another 24 h cell incubation. After being rinsed twice, the cells were fixed with 0.5 mL 4% formaldehyde for Hoechst 33,258 (nuclei, blue) staining. After the slides were stained and sealed, the fluorescence images were taken.

Similarly, HepG2 cells were seeded in 24-well plates at a density of 1×10^5 cells/well; the plates were then placed in a cell incubator until all cells adhered to the well bottoms. Treatments were then conducted with Au@Bi_2S_3-PVP/DOX. After a 12 h incubation, the incubation solution was replaced with fresh medium, and the cells were irradiated with an 808 nm laser for 3 min at an output power density of 1.45 W/cm^2. Finally, calcein acetoxy-methyl ester (Calcein AM) and PI were applied to stain all the cells.

2.14. In vitro cell migration assays

After being seeded in six-well plates at a density of 3×10^5 cells/well, HepG2 cells were placed in a cell incubator for 24 h and allowed to adhere to the well bottoms. With a 10 μL pipette tip, scratch lines were made every 0.8 cm vertically through the formed monolayer, and the culture medium was then removed; this was followed by three washes with PBS to eliminate floating cells. Afterward, the cultured cells were incubated in 1% FBS containing 1% DMSO, Au@Bi_2S_3-PVP,

DOX, Au@Bi_2S_3-PVP/DOX, Au@Bi_2S_3-PVP + NIR and Au@Bi_2S_3-PVP/DOX + NIR with the same concentration (5 μM). The migration imaging for each group was sequentially captured at 6 h, 12 h and 24 h. Equation (4) shows the calculation of the cell migration rate in each group:

$$\text{Migration rate} = (Wa / Wc) \times 100\% \quad (4)$$

where *W*c and *W*a refer to the migration distance of the control group and the analyzed group, respectively.

2.15. In vitro colony formation assays

HepG2 cells were seeded in six-well plates with a cell density 400 cells/well and incubated in culture medium containing 1% DMSO and 20 μg mL^{-1} of Au@Bi_2S_3-PVP, DOX, Au@Bi_2S_3-/PVP/DOX, Au@Bi_2S_3-PVP + NIR and Au@Bi_2S_3-PVP/DOX + NIR. More than 50 cells were needed for colony counting. After seeding, the number of colonies was recorded on the 7th day. The calculation of the colony formation rate was according to equation (5) below:

$$\text{Colony formation rate} = (\text{number of colonies/number of seeded cells}) \times 100\% \quad (5)$$

Each treatment was carried out in quintuplicate.

2.16. In vivo infrared thermal imaging

All animal experiments were carried out under the approval of the China Committee for Research and Animal Ethics in compliance with the laws pertaining to experimental animals. First, two mice were injected with 10% trichloroacetaldehyde hydrate (40 mg/kg) for anaesthetization. Subsequently, 100 μL 500 μg mL^{-1} Au@Bi_2S_3-PVP NBs was administered to the mice through caudal vein injection, and PBS was used as a control. One hour after the mice were injected, the tumor area was irradiated with an 808 nm laser for 3 min. The output power densities were set to 0.8 W/cm^2 and 1.45 W/cm^2. The temperature was recorded every 1 min *via* an FLIR System.

2.17. In vivo PTT of tumors

HepG2 cells were subcutaneously inoculated in the right side of the scapula in the selected BALB/c nude mice at a dose of 1.2 × 10^6 cells per mouse. All mice were fed for 3–5 weeks until the tumors grew to a diameter of 8–10 mm, and then two mice were anaesthetized by injection of 10% trichloroacetaldehyde hydrate (40 mg/kg). One mouse was treated with 100 μL 500 μg mL^{-1} Au@Bi_2S_3-PVP NBs, and a second was treated with 100 μL PBS as a control. One hour later, the mice in each group were irradiated with an 808 nm laser at the output power density of 0.8 W/cm^2 or 1.45 W/cm^2 for 3 min. Finally, all mice were scarified for tumor removal. The tumors were subsequently embedded in paraffin and cryosectioned into 6 μm slices which were stained with hematoxylin/eosin for examination. The images were captured with a Nikon TE2000-U inverted fluorescence microscope.

2.18. In vivo PA/CT imaging

After the HepG2 cells (about 1.2 × 10^6 cells/mouse) were subcutaneously injected into the female BALB/c nude mice, 3–5 weeks' feeding was required to allow the tumors to grow to 7–8 mm in diameter. Before CT scanning, 100 μL of 500 μg mL^{-1} Au@Bi_2S_3-PVP NBs was administered to the mice through the tail vein (TV) or through intratumoral (IT) injection, with saline as a control. To anesthetize the mice, 10% trichloroacetaldehyde hydrate was used at a dosage of 40 mg/kg body weight. At 1 h after injection, the CT imaging was performed.

The PA imaging was conducted with an animal PA imaging system (Vevo LAZR-X, USA). Through both TV and IT injection, 100 μL Au@Bi_2S_3-PVP NBs were administered to HepG2 tumor-bearing BALB/c nude mice, and PBS was used as a control. The mice were anesthetized with isoflurane before the PA images were recorded. The NIR-I window ranging from 680 to 970 nm was set as the excitation wavelength with 10 nm intervals. The PA signal intensity of the tumor site was detected at different times: pre-injection, 2 h, 4 h and 6 h.

2.19. In vivo antitumor effects

1.2 × 10^6 HepG2 cells were subcutaneously inoculated in the right side of the scapula of each BALB/c nude mouse, which had been fed for 3–5 weeks to achieve a tumor diameter of 6–7 mm. The mice were then divided into six groups: 1) PBS, 2) Au@Bi_2S_3-PVP NBs, 3) DOX, 4) Au@Bi_2S_3-PVP/DOX, 5) Au@Bi_2S_3-PVP + NIR and 6) Au@Bi_2S_3-PVP/DOX + NIR. Each group contained five replicate mice to minimize the differences in tumor sizes. Then 100 μL of the examined materials at different concentrations was administered through TV injection for each group (Au@Bi_2S_3-PVP NB based materials, 2 mg/kg; DOX, 0.4 mg/kg). For groups 5 and 6, 1 h after the injection, an 808 nm laser was used to irradiate the tumor area with a power density of 1.45 W/cm^2 for 3 min for PTT. The mice in each group were injected on days 0 and 6. When the therapy ended, the mice were dissected to collect the tumors, which were photographed and weighed successively. At the same time, the hearts, livers, spleens, lungs and kidneys were also collected and preserved in 4% formaldehyde for the subsequent examination of the biological toxicity of the target materials.

2.20. In vivo pharmacokinetics

A total of 100 μL of 2 mg/kg Au@Bi_2S_3-PVP NBs was administered through TV injection into HepG2 tumor-bearing BALB/c nude mice. Then, the blood was collected from the orbital vein at various time points (2 min, 5 min, 10 min, 30 min, 1 h, 2 h, 4 h, 6 h or 12 h) to determine the gold concentration in the blood by ICP-MS.

2.21. Blood routine analysis and biochemistry

HepG2 tumor-bearing BALB/c nude mice were divided into six groups: 1) PBS, 2) Au@Bi_2S_3-PVP NBs, 3) DOX, 4) Au@Bi_2S_3-PVP/DOX, 5) Au@Bi_2S_3-PVP + NIR and 6) Au@Bi_2S_3-PVP/DOX + NIR. Each group contained three mice to minimize the inter-individual differences. A total of 100 μL of the examined material was then administered through TV injection for each group (Au@Bi_2S_3-PVP NBs based material, 2 mg/kg; DOX, 0.4 mg/kg). For groups 5 and 6, 1 h after the injection, an 808 nm laser was used to irradiate the tumor area with a power density of 1.45 W/cm^2 for 3 min. The mice in each group were injected on days 0 and 6. The blood was collected after the therapy ended.

2.22. Statistical analysis

Experimental data were compared in Prism software. The results obtained are expressed as the mean ± standard deviation (S.D.) and were considered statistically significant when *p < 0.03, **p < 0.002, ***p < 0.0002 or ****p < 0.0001.

3. Results and discussion

3.1. Synthesis and characterization of Au@Bi_2S_3 NBs

Since the first demonstration by Murphy et al. CTAB, a cationic surfactant, has been shown to improve seed-mediated growth more effectively and thus has been widely used in the preparation of Au NRs [37,38]. The Au NRs were synthesized through this method. However, to tune the aspect ratio of Au NRs to achieve a greater longitudinal

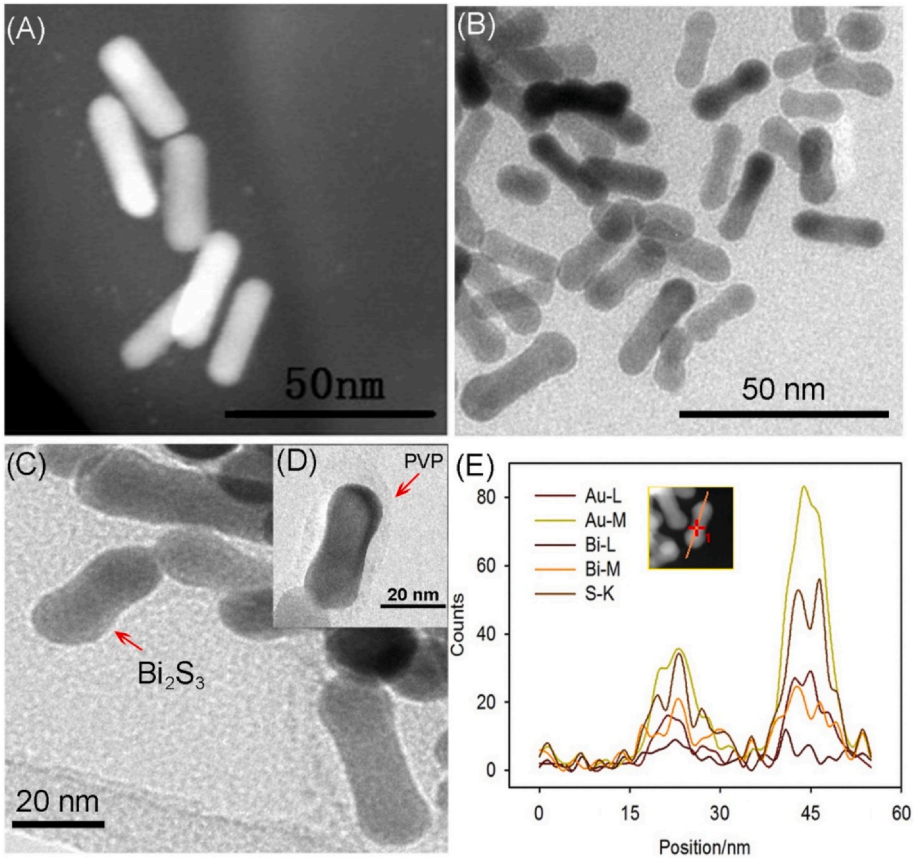

Fig. 1. TEM images of A) initial Au NRs, B and C) Au@Bi_2S_3 NBs and D) Au@Bi_2S_3-PVP NBs; E) scanning position; and EDS spectrum of Au@Bi_2S_3 NBs.

surface plasmon resonance (L-SPR) than 700 nm, 5-bromosalicylic acid was used as an additive. Fig. 1A shows an L-SPR of Au NRs greater than 700 nm, which was mainly ascribed to the large aspect ratio exceeding 3.0. The concentration of CTAB used here was 0.05 M, and the concentrations of other additives such as $AgNO_3$ were optimized to reduce the viscosity of Au NR growth solution for better solute diffusion and to control the reshaping of CTAB-stabilized Au NRs to bone-like NRs. The amount of $AgNO_3$ used not only significantly influences the maximum length obtainable [39] but also exhibits appreciable effects on the yield and dimensions of the Au NRs in the presence of Br^- ions from CTAB [40–42]. Generally, the large lattice mismatch between S and Au makes the growth of semiconductor sulfide shells on Au NRs difficult [43]. Through a one-pot reaction, however, the sulfide shell can easily form on the surfaces of Au NRs. The cooperative effects of CTAB, AA and S source (TAA) were studied on the formation of typical bone-like morphology. The co-promoting effect of CTAB and TAA was considered to substantially contribute to the formation of the morphology of Au@Bi_2S_3 NBs. CTAB has previously been revealed to bind much more strongly to the side facets than the ends of Au NRs, thus leading to a higher overgrowth rate of semiconductor shell along the ends than along the side facets [44]. AA not only serves as a reducing agent for the directed overgrowth of Au but also facilitates the growth of a sulfide shell. According to a previous report [45], AA assists in the deposition of dense and complete semiconductor shells on metallic NPs. The combination of a sulfide (S) source from TAA with Bi^{3+} generates a complex and then transports the metallic ions to the Au surface through cooperation with CTAB, thus leading to the growth of Bi_2S_3 shells on the surfaces of Au NRs. Therefore, regardless of the size of the lattice mismatch (as for Au@Bi_2S_3 NBs: 2–3%), the Bi_2S_3 nanoshell formed outside the Au NRs [46]. The morphology of the Au@Bi_2S_3 NBs was viewed under different magnifications (from 50 nm to 20 nm), as shown in Fig. 1B and C. Moreover, the PVP modification formed a vague shell on the surfaces of Au–Bi_2S_3 NBs, which did not obviously change the shape of the Au@Bi_2S_3 NBs (Fig. 1D). The composition and structure of the as synthesized Au@Bi_2S_3 NBs were measured by performing elemental linear screening through energy-dispersive X-ray spectroscopy (EDS) (Fig. 1E), and the transverse surface distributions of Au, Bi and S were clearly observed across the Au@Bi_2S_3 NBs.

3.2. XPS analysis of Au@Bi_2S_3-PVP NBs

The chemical composition of Au@Bi_2S_3-PVP NBs was determined *via* XPS analysis. The fitted spectrum of Au4f in Fig. 2A displayed two typical peaks ($Au4f_{5/2}$ and $Au4f_{7/2}$) of the elemental Au at the binding energies of 87.35eV and 83.67 eV, respectively, indicating the presence of Au NRs. In Fig. 2B, peaks of $Bi4f_{5/2}$ (164.15 eV and 158.74 eV) and $Bi4f_{7/2}$ (163.11eV, 157.80 eV) were clearly observed and were ascribed to the binding of Bi with S in the structure of Bi_2S_3. The peak at 160.97 eV might have been from the trace byproduct, Bi_2O_3. In the fitted spectrum of S2p (Fig. 2C), the peaks corresponding to $S2p_{1/2}$ (164.16 eV and 158.69 eV) and $S2p_{3/2}$ (163.12 eV and 157.70 eV) verified the formation of a Bi_2S_3 shell. The small peak at 161.00 eV might have been due to the formation of trace Au–S bonds, a possibility supported by the small peak of the Au–S bond at 85.32 eV in the fitted spectrum of Au4f. The existence of C–C, C–N and C═O bonds inside Au@Bi_2S_3-PVP NBs was confirmed by three peaks at 284.78 eV, 285.95 eV and 287.60 eV, respectively (Fig. 2D). Fig. 2E shows the fitted spectrum of N1s, in which both N–C and N–H bonds from PVP were clearly observed at 399.61 eV and 401.91 eV. In addition, in Fig. 2F, the peak of C═O was observed at 531.85 eV, and the other two peaks at 532.55 eV and 530.95 eV were probably from the adsorbed O_2 and trace Bi_2O_3 inside the Au@Bi_2S_3-PVP NBs. All the obtained results revealed the formation of Au@Bi_2S_3 NBs and the successful modification of PVP on their surfaces.

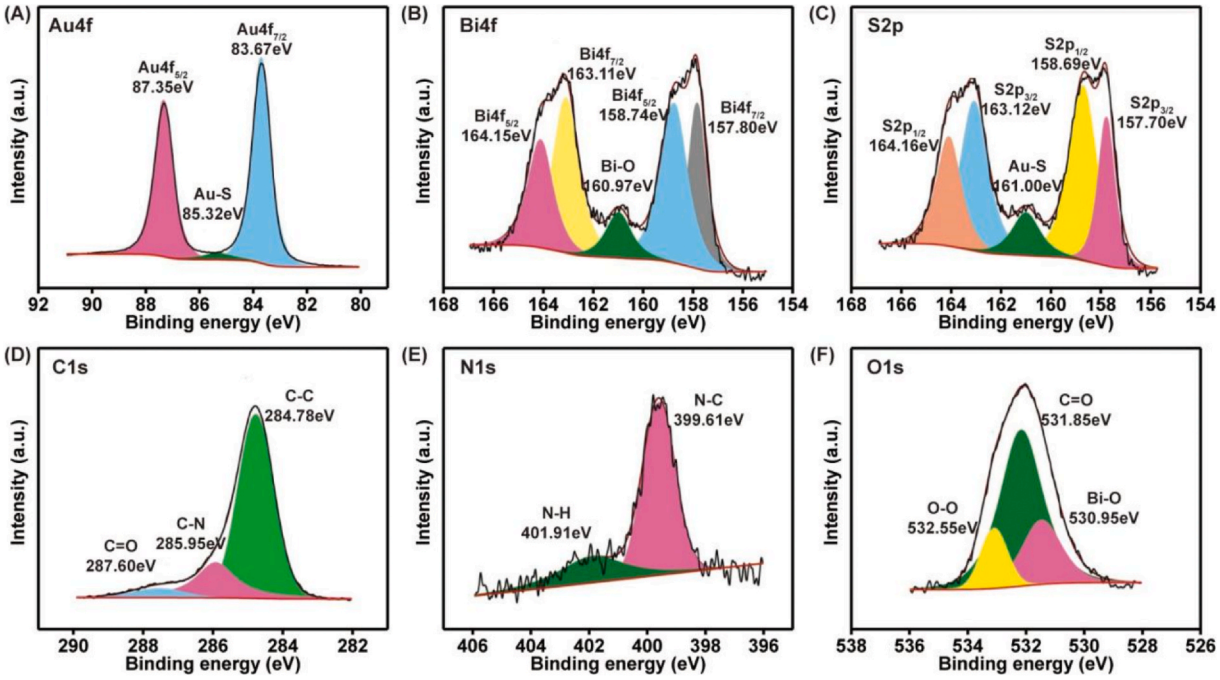

Fig. 2. XPS fitted spectra of A) Au4f, B) Bi4f, C) S2p, D) C1s, E) N1s and F) O1s in Au@Bi_2S_3-PVP NBs.

3.3. Surface plasmon enhancement and physiological stability of Au@Bi_2S_3 NBs

To further confirm the formation of Au@Bi_2S_3 NBs, we first synthesized Bi_2S_3 NRs according to a previously reported method for comparison, and the variations in the extinction spectra of Au NRs, Bi_2S_3 NRs, Au + Bi_2S_3 NRs and Au@Bi_2S_3 NBs were obtained, as shown in Fig. 3A, and found to be dependent on the shape of Au NRs and the Bi_2S_3 nanoshell. The Au NRs had two clear absorption peaks at 531 nm and 749 nm (black curve). For the initial Au NRs, the extinction band around 530 nm corresponded to the transverse SPR (T-SPR), and another at ~750 nm belonged to the L-SPR. Only a weak absorption peak was present around 500 nm for Bi_2S_3 NRs (red curve). For the mixture of Au + Bi_2S_3 NRs, two absorption peaks appeared at 515 and 749 nm (blue curve), results almost the same as those for Au NRs, and the slight blue shift to 515 nm was probably caused by the overlay of adsorption and interaction between Au NRs and Bi_2S_3 NRs. After Au NR cores were coated with Bi_2S_3, we expected the Au@Bi_2S_3 NBs to demonstrate SPR absorption. Interestingly, both T-SPR and L-SPR absorptions still clearly appeared, and a red-shift to approximately 820 nm accompanied by a ~2.0 times intensity enhancement was observed for the L-SPR wavelength (green curve). The increasing refractive index of the surrounding medium as a result of Bi_2S_3 coating was believed to mainly cause the red-shift of the L-SPR wavelength [47], and the local field enhancement from the Au NR surface plasmon coupling probably led to the enhanced absorption of Au@Bi_2S_3 NBs [48,49]. The formation of Au@Bi_2S_3 NBs and not the simple mixture of Au + Bi_2S_3 NRs was further verified.

In addition, the physiological stability of Au@Bi_2S_3 NBs was investigated in different solutions including doubly distilled water, PBS (pH 7.4) and DMEM (containing 10% FBS and 1% PS), and their time-dependent HDs were measured daily within the first 7 days as the key criterion to assess the stability. Au@Bi_2S_3 NBs were well dispersed in all three solutions, and no obvious aggregation was observed after the 7-day incubation, as reflected in the clearly constant HD of Au@Bi_2S_3 NBs (Fig. 3B). The results indicated that Au@Bi_2S_3 NBs displayed excellent physiological stability in doubly distilled water, PBS and DMEM.

3.4. Properties of Au@Bi_2S_3 NBs after PVP modification

As mentioned above (Figs. 1D and 2), a vague shell was clearly observed on the surfaces of Au@Bi_2S_3 NBs as a result of the successful PVP modification. In addition, as compared with Au@Bi_2S_3 NBs without PVP, the appearance of obviously enhanced peaks of C1s, N1s and O1s confirmed the presence of PVP on the surfaces of Au@Bi_2S_3-PVP NBs, as shown in Fig. 3C. After the modification of PVP, a typical amphiphilic polymer used to improve the biocompatibility of Au@Bi_2S_3 NBs and DOX loading, DOX easily adsorbed to the surfaces of Au@Bi_2S_3-PVP NBs with improved aqueous dispersibility due to the electrostatic interaction. The measurement of the contact angle before (~65.5°) and after (~20.8°) the modification of PVP verified the clearly improved hydrophilicity of Au@Bi_2S_3 NBs, as a result of the formation of a PVP layer (Fig. 3D). More importantly, in cancer treatment, the use of Au@Bi_2S_3-PVP NBs is required to have high biocompatibility. The influence of the Au@Bi_2S_3 NBs with or without PVP on the viability of cancer cells was therefore investigated to further assess their biocompatibility *in vitro* (Fig. 3E). First, both Au@Bi_2S_3 NBs and Au@Bi_2S_3-PVP NBs at different concentrations (1, 5, 10, 25, 50, 100, 150 and 300 μg mL^{-1}) were incubated with HepG2 cells for 24 h, and then the cell viability was tested *via* MTT assays. No adverse effects on cell viability were observed after PVP modification, even at concentrations as high as 300 μg mL^{-1}, thus revealing the low cytotoxicity of the Au@Bi_2S_3-PVP NBs. In addition, the blood compatibility of Au@Bi_2S_3-PVP NBs was evaluated through hemolysis assays of RBCs (Fig. 3F). The hemolytic behavior of the Au@Bi_2S_3-PVP NBs was investigated at varying concentrations up to 400 μg mL^{-1}, and doubly distilled water and PBS were selected as positive and negative controls, respectively, according to a previously described protocol [50]. A ten-fold dilution of fresh blood stabilized with EDTA was used to prepare suspensions of RBCs in PBS. At 570 nm, the UV–Vis absorbance of the supernatant was determined to calculate the concentration of hemoglobin released by the hemolyzed RBCs. At concentrations from 20 to 400 μg mL^{-1}, the RBC hemolysis was negligible between the Au@Bi_2S_3 NBs with or without PVP (Fig. 3E), thus suggesting that both Au@Bi_2S_3 NBs and Au@Bi_2S_3-PVP NBs have excellent blood compatibility [50]. Moreover, the PVP modification clearly increased the blood compatibility of Au@Bi_2S_3-PVP NBs. The observed favorable blood compatibility was

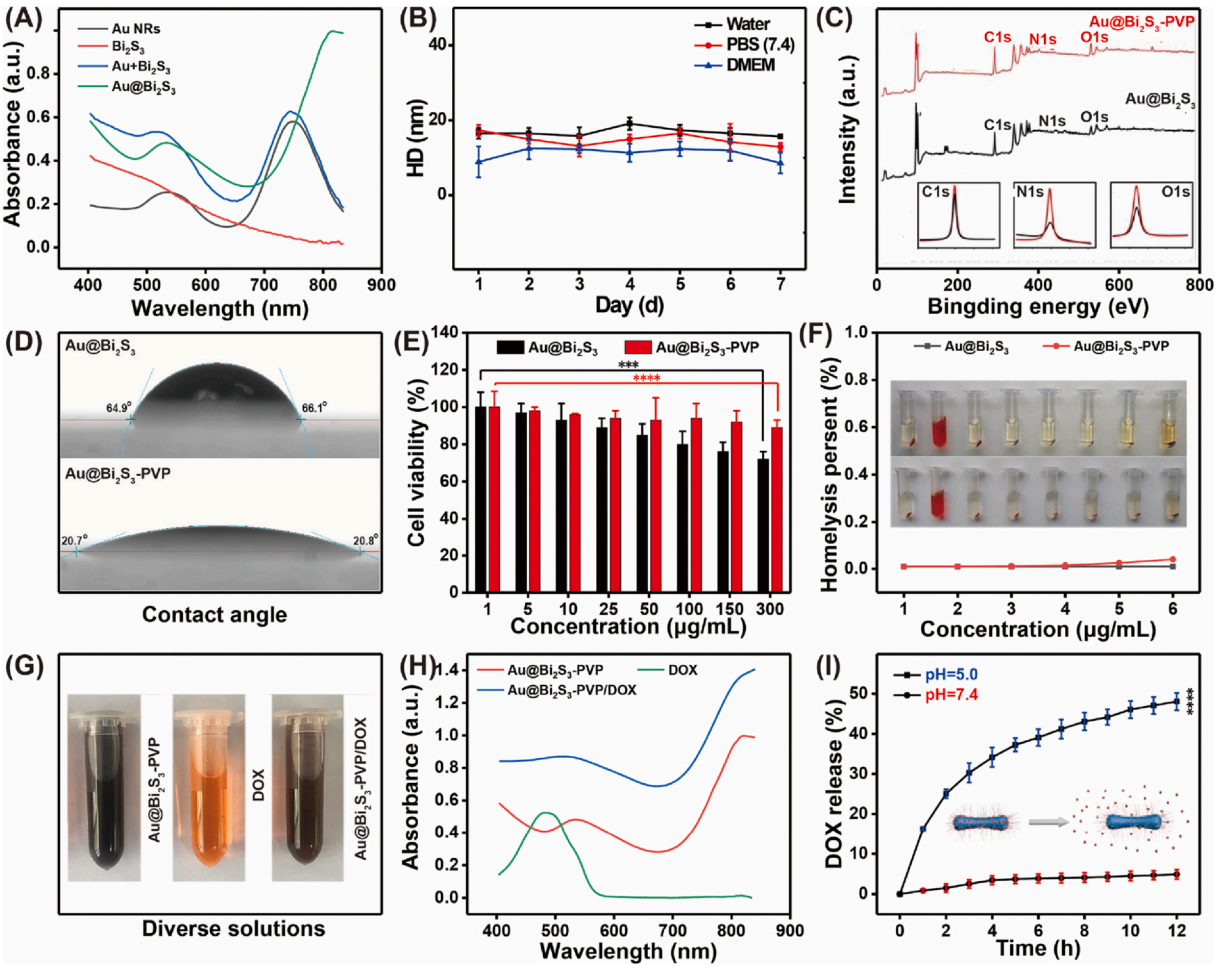

Fig. 3. A) UV–Vis spectra of Au NRs, Bi_2S_3 NRs, Au + Bi_2S_3 NRs and Au@Bi_2S_3-PVP NBs; B) physiological stability of Au@Bi_2S_3-PVP NBs in doubly distilled water, PBS (pH 7.4) and DMEM; C) XPS survey spectra and D) contact angles of both Au@Bi_2S_3 NBs and Au@Bi_2S_3-PVP NBs; E) the viability of HepG2 cells and F) the hemolytic percentage of RBCs (*inset*: images of hemolysis in each group) incubated with the Au@Bi_2S_3 NBs and Au@Bi_2S_3-PVP NBs at various concentrations (doubly distilled water: positive control; PBS: negative control); G) different colors and H) UV–Vis spectra of Au@Bi_2S_3-PVP NBs, DOX and Au@Bi_2S_3-PVP/DOX; I) the cumulative release profiles of Au@Bi_2S_3-PVP/DOX in PBS (pH 7.4) and HAc/NaAc solution (pH 5.0). Data are expressed as mean ± standard deviation of five replicates (*p < 0.03, **p < 0.002, ***p < 0.0002 and ****p < 0.0001).

comparable to that of reported polyethylene glycol (PEG)-modified mesoporous silica nanoparticles [50], thus supporting safety in biomedical applications.

As discussed, PVP modification improves DOX loading, because of ready adsorption to the surfaces of Au@Bi_2S_3-PVP NBs through electrostatic interactions. Thus, by mixing solutions of DOX (orange) with the core-shell Au@Bi_2S_3-PVP NBs (dark brown) for 24 h at room temperature, DOX loaded Au@Bi_2S_3 nanocomposites (Au@Bi_2S_3-PVP/DOX) (brown) formed (Fig. 3G), as verified through UV–Vis spectra (Fig. 3H). DOX exhibited substantial absorbance in the UV–Vis region at ~490 nm, whereas the as-formed Au@Bi_2S_3-PVP/DOX showed not only the plasma absorption band of Au@Bi_2S_3-PVP NBs but also the typical absorption peak of DOX, thus revealing the successful incorporation of DOX into Au@Bi_2S_3-PVP NBs. High encapsulation efficiency (74.0%) and loading content (15.6%) were obtained for the DOX incorporated Au@Bi_2S_3-PVP NBs, which were comparable to those of the previously reported Au@$mSiO_2$ core-shell nanostructures (67.8% and 14.5%) [51]. Moreover, in PBS (pH 7.4) and acetate buffer (HAc/NaAc, pH 5.0), the corresponding cumulative DOX release within 12 h was investigated, as shown in Fig. 3I. At pH 5.0, the nanocomposites showed a rapid release of DOX (26% of drug released) in the first 3 h and a sustained relatively slow release afterward (red curve). The drug release rate within 12 h was calculated to be as high as 48%. By comparison, the release rate of DOX was much lower in PBS (yellow curve), with less than 5% of DOX released within 12 h. The different release rates of DOX were attributed primarily to the protonation/deprotonation of PVP, a pH sensitive amphiphilic polymer, which can undergo a protonation/deprotonation switch under different pH conditions. DOX, a cationic anticancer drug, was easily attracted to the surface of PVP-modified Au@Bi_2S_3 NBs under neutral conditions, owing to the strong electrostatic interaction between PVP and DOX, and was partly released in lower pH media [52,53]. Thus, the Au@Bi_2S_3-PVP NBs displayed promising pH sensitive drug release, owing to the variations in the electrostatic attraction between Au@Bi_2S_3-PVP NBs and drug molecules in different pH media [54], thus increasing the accumulation of DOX in the cytoplasm of HepG2 cancer cells and decreasing DOX release in healthy tissues. The drug delivery performance of Au@Bi_2S_3-PVP NBs was compared with that of several previously reported Bi-based nanomaterials (Table 1). Usually, the encapsulation efficiency of a drug is used to evaluate the drug delivery performance of nanomaterials. The Au@Bi_2S_3-PVP NBs clearly showed a drug encapsulation efficiency comparable to those of the listed Bi-based materials. Moreover, in the simulated tumor microenvironment (pH 5.0), Au@Bi_2S_3-PVP/DOX exhibited a higher DOX release rate (46% within 10 h) than the reported membrane-camouflaged quercetin-loaded hollow bismuth selenide nanoparticles (M@BS-QE NPs, ~40% within 10 h) [55]. Although DOX is a clinically effective anticancer drug, adequate doses during cancer therapy unavoidably produce severe side effects. However, the more

Table 1
Comparison of Au@Bi_2S_3 NBs with other Bi-based nanomaterials in terms of particle size, PTT, bioimaging and drug loading performance.

Name	Particle size	PCE (η)	Bioimaging	Drug loading capacity	Refs.
Bi_2S_3 NRs	50 nm (length) 10 nm (width)	~28.1%	yes	–	[56]
Bi_2S_3–Au NRs	60 ± 5 nm (length) 15 ± 2 nm (width)	51.06%	yes	–	[32]
Bi_2S_3-PEG Nus	~137 nm	~18.3%	yes	~37.9%	[57]
Tam-Bi_2S_3@mPS	130 nm (length) 60 nm (width)	29.53%	yes	60.85%	[58]
Bi-BSA NRs	~134 nm	~27.1%	yes	69%	[59]
Bi_2Se_3@mSiO_2-PEG NPs	~60.5 nm	~30.5%	no	~50%	[60]
Bi_2WO_6-DOX-PEG NSs	~117 nm (lateral size) ~2.4 nm (thickness)	36.5%	yes	81.3%	[61]
Bi_2S_3@MSN NPs	~100 nm	36.62%	yes	99.85%	[62]
Au@Bi_2S_3 NBs	~41 nm (length) 12 nm (width)	~68.1%	yes	74.0%	This work

Note: Bi_2S_3 NRs: Bi_2S_3 nanorods; Bi_2S_3–Au NRs: Bi_2S_3–Au nanorods; Bi_2S_3-PEG Nus: PEGylated Bi_2S_3 nano-urchins; Tam-Bi_2S_3@mPS: trastuzumab-Bi_2S_3@mesoporous silica; Bi-BSA NRs: bovine serum albumin modified Bi nanoraspberries; Bi_2Se_3@mSiO_2-PEG NPs: PEG modified mesoporous silica-coated Bi_2Se_3 nanoparticles; Bi_2WO_6-DOX-PEG NSs: PEGylated and DOX-loaded Bi_2WO_6 nanosheets; Bi_2S_3@MSN NPs: mesoporous silica-coated Bi_2S_3 nanoparticles.

effective accumulation of DOX in HepG2 cancer cells and the lower amount of released DOX in normal tissues accordingly enhanced the long-term therapeutic efficacy and decreased toxicity.

3.5. Cell uptake of Au@Bi_2S_3-PVP/DOX NBs

Cell uptake of Au@Bi_2S_3-PVP/DOX NBs was examined by recording the fluorescence images of HepG2 cells treated with PBS, DOX and Au@Bi_2S_3-PVP/DOX for 2 h, to evaluate the intracellular drug delivery of Au@Bi_2S_3-PVP NBs (Fig. 4). After being stained with DAPI (blue fluorescence), HepG2 cells incubated with DOX loaded Au@Bi_2S_3-PVP NBs were observed under an inverted fluorescence microscope. As shown in the fluorescence images in Fig. 4, compared with the control results, weak red fluorescence was observed in the merge fluorescence image of HepG2 cells treated with DOX only, thus indicating that only a small amount of free DOX entered the cells. In contrast, after the incubation of HepG2 cells with Au@Bi_2S_3-PVP/DOX, the nuclei of HepG2 cells exhibited remarkably enhanced red fluorescence, which was ascribed to the increasing amount of DOX taken up into the nuclear region of HepG2 cells, thus revealing the efficient cellular uptake of Au@Bi_2S_3-PVP NBs. These results strongly indicated that the Au@Bi_2S_3-PVP NBs can effectively deliver DOX into HepG2 cancer cells and show great potential as drug carriers for cancer treatments [60,63].

3.6. PT performance

PT agents can be used to damage or even kill cancer cells at specific tumor sites by locally converting photons into heat during PTT for cancer. Au@Bi_2S_3 NBs were regarded as good nanoheaters for tumor ablation because of their remarkable NIR absorbance. Under the NIR irradiation of an 808 nm laser (at a power density of 1.45 W/cm^2), the temperature changes of 1.0 mL Au@Bi_2S_3 NB solution were detected at different concentrations varying from 6.25 to 100 ppm. After each solution was irradiated for 5 min, the temperature elevation for all Au@

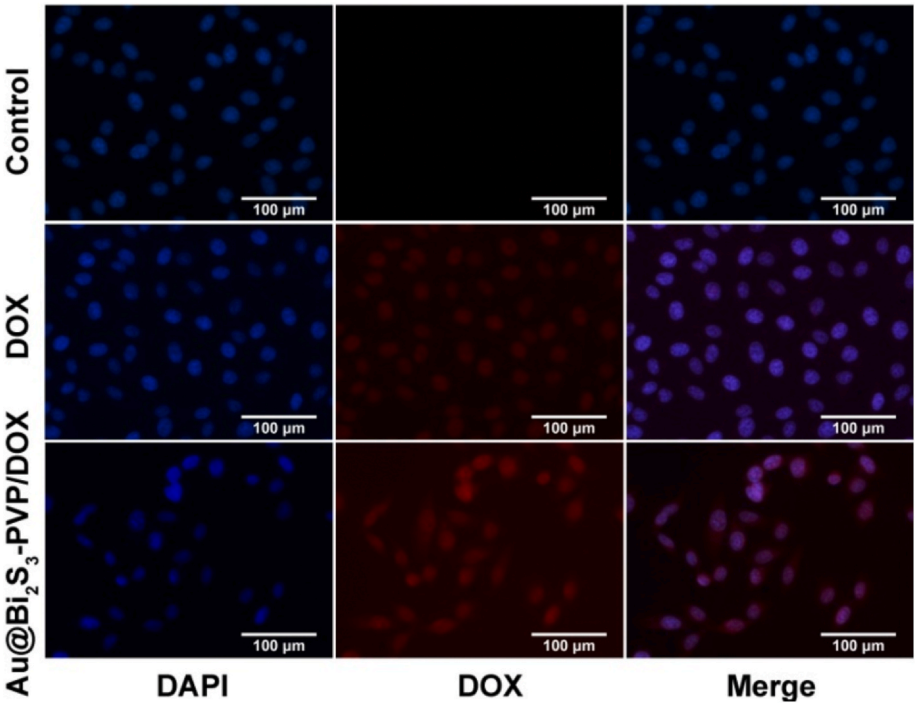

Fig. 4. Fluorescence images of HepG2 cells treated with PBS, DOX and Au@Bi_2S_3-PVP/DOX for 2 h. Red fluorescence: DOX; blue fluorescence: cell nuclei after DAPI staining. Scale bar: 100 μm.

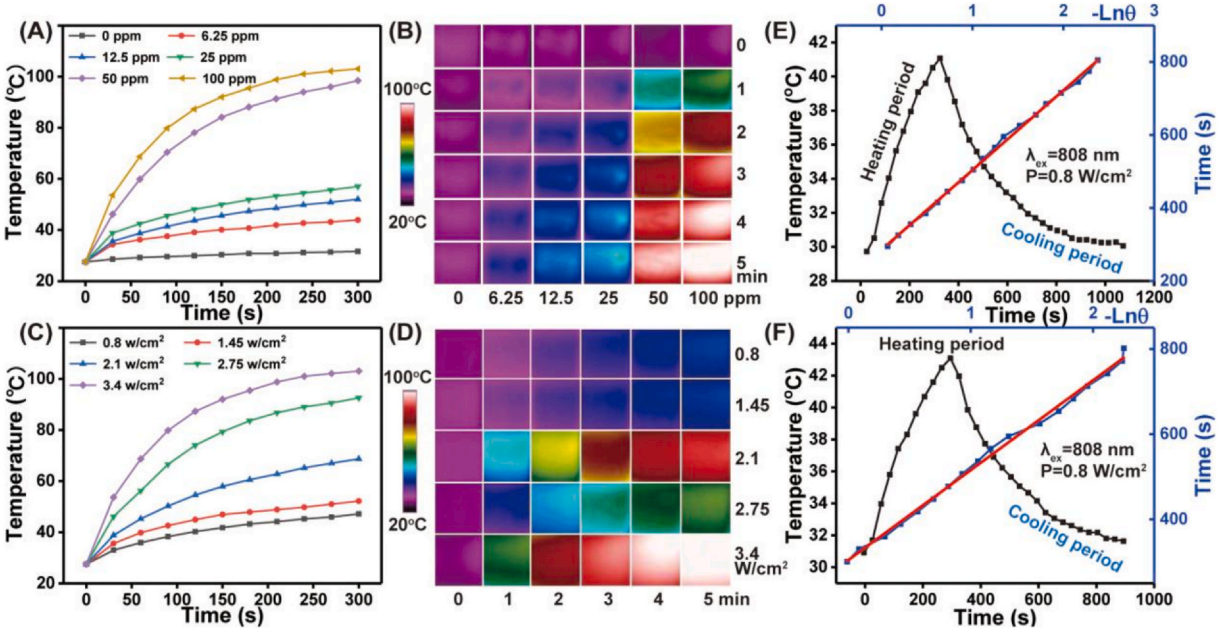

Fig. 5. Temperature increase curves of A) doubly distilled water and Au@Bi_2S_3 NB solution at concentrations from 6.25 to 100 ppm, and C) 100 ppm Au@Bi_2S_3 NB solution irradiated with an 808 nm laser (at power density varying from 0 to 3.4 W/cm^2); B and D) different laser power densities under 808 nm laser irradiation with a concentration of 100 ppm versus irradiation time; typical temperature curves of the aqueous solutions of E) Au NRs and F) Au@Bi_2S_3 NBs versus time (laser on for 5 min and then laser off; doubly distilled water as control); the measurement of the time constant for the system heat transfer used the linear regression of the cooling profile of E) Au NRs and F) Au@Bi_2S_3 NBs.

Bi_2S_3 NB solutions increased from 4.2 to 72.5 °C. However, the doubly distilled water showed a small temperature change under the same power density (Fig. 5A and C). Therefore, the temperature variation showed a strong dependence on the concentration of Au@Bi_2S_3 NB solutions. When the concentration of Au@Bi_2S_3 NBs was 100 ppm, the temperature increase was clearly dependent on the power density (Fig. 5B and D). With an increase in the laser function power density from 0 to 3.4 W/cm^2, the solution's temperature increased by 18.5, 24.1, 41.4, 65.7 and 72.5 °C, after the 5 min irradiation. After irradiation, the final temperature was sufficiently high to burn the cancer cells to death. The η of Au@Bi_2S_3 NBs was calculated to be as high as 68.1%, according to a previously described method [64–66] (Fig. 5F), much higher than that of Au NRs (49.1%, Fig. 5E) and many existing nanomaterials used as PT agents [64–71]. Several other Bi-based nanomaterials were compared with Au@Bi_2S_3 NBs in tumor PTT (Table 1). The Au@Bi_2S_3 NBs performed better in PTT because of the ultrahigh PCE among the listed materials (and significantly higher than 45.3% for Bi-SR-PEG and 51.06% for Bi_2S_3–Au NRs [32,72]). Briefly, η was calculated with equation (6) below:

$$\eta = \frac{hS(T\max,\mathrm{dis} - T\mathrm{surr,\ water})}{I(1 - 10^{-A_{808}})} \quad (6)$$

where h, S, I and A_{808} refer to the heat transfer coefficient, the surface area of the sample container, the laser power density and the absorbance of dispersion at the wavelength of 808 nm, respectively. $\triangle T_{max,\ diss}$ and $\triangle T_{surr,\ water}$ correspond to the temperature changes of the sample dispersions and doubly distilled water at the maximum equilibrium temperature. The temperature decrease was recorded immediately after the light source was turned off and was used to calculate the value of hS in the equation (Fig. 5E and F). Thus, the Au@Bi_2S_3 NBs exhibited a greatly improved PCE after being coated with Bi_2S_3, probably as a result of the release of heat radiation caused by the recombination of excited electrons with electron-holes inside Bi_2S_3 in the presence of Au NRs under NIR radiation. These results confirmed that the introduction of Bi_2S_3 markedly enhanced the adsorption of Au NRs in the NIR region. Because cancer cells can be efficiently eliminated by such hyperthermia in a short time [73], Au@Bi_2S_3 NBs were thus presumed to be a suitable agent for PTT treatment of cancers. In addition, no obvious difference in temperature change was observed for the Au@Bi_2S_3 NB solutions among three PT measurements, thus revealing the excellent photostability.

3.7. In vivo PT imaging and in vitro inhibition behavior

The injected areas of two mice were perpendicularly irradiated under power densities of 0.8 W/cm^2 and 1.45 W/cm^2 with an 808 nm semiconductor laser. After 3 min laser irradiation, both the infrared thermal imaging and the temperature were recorded (Fig. 6). As shown in Fig. 6A, before irradiation, a light blue color over the whole mouse body clearly indicated a uniform temperature distribution in the two mice, which completely disappeared, owing to the dramatically changing color, after laser irradiation. After being individually irradiated with 0.8 and 1.45 W/cm^2 for 3 min, the tumor regions injected with Au@Bi_2S_3-PVP NBs changed from green to red and became larger, whereas the tumor region injected with PBS became sky blue, as compared with the color after irradiation by 0 W/cm^2. The Au@Bi_2S_3-PVP NB-injected tumor area was heated to 45 °C and 52 °C very quickly after 3-min irradiation under an output power density of 0.8 W/cm^2 and 1.45 W/cm^2, respectively, a temperature sufficiently high to kill the cancer cells *in vivo*. Moreover, both the increase rate and the attainable maximum of temperature of the Au@Bi_2S_3-PVP NBs were higher than those of Bi_2S_3-PEG Nus and gadolinium-chelate functionalized and PEG-modified Bi nanoparticles (Gd-PEG-Bi NPs) [74,75]. In contrast, the tumor temperature increased by less than 5 °C for the control mouse after receiving the same irradiation treatment. Therefore, both the temperature and color changes around tumor cells were detected through infrared thermal imaging of the Au@Bi_2S_3-PVP NBs irradiated with the 808 nm NIR laser.

The effects of the individual PTT and chemotherapy, as well as their *in vitro* combination, were evaluated by culturing HepG2 cells in a series of media containing the same amounts of Au@Bi_2S_3-PVP NBs, free DOX, Au@Bi_2S_3-PVP/DOX, Au@Bi_2S_3-PVP NBs and Au@Bi_2S_3-PVP/DOX under NIR laser irradiation (Au@Bi_2S_3-PVP + NIR, Au@Bi_2S_3-PVP/DOX + NIR). An equivalent dosage was applied to each

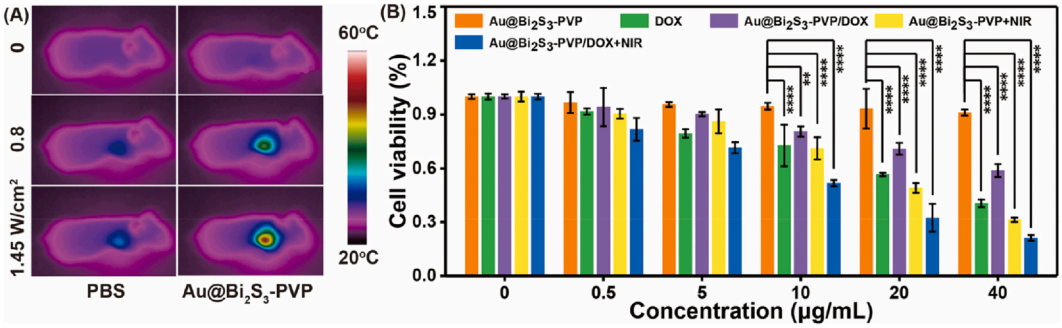

Fig. 6. A) Infrared thermal imaging of two mice administered Au@Bi_2S_3 NBs (right) or PBS (left) *via* TV injection, exposed to an 808 nm laser (0.8 W/cm^2 and 1.45 W/cm^2) for 3 min. B) The cell viability of Au@Bi_2S_3 NBs, free DOX, Au@Bi_2S_3-DOX, Au@Bi_2S_3 + NIR and Au@Bi_2S_3-DOX + NIR incubated with HepG2 cells at different concentrations. An 808 nm laser was used to perform the NIR irradiation for 3 min. Data are expressed as mean ± standard deviation of five replicates (*p < 0.03, **p < 0.002, ***p < 0.0002 and ****p < 0.0001).

group for the evaluation of cell viability *via* MTT assays. Fig. 6B shows that the cell viability clearly decreased when the material concentration increased in all groups except for the Au@Bi_2S_3-PVP NBs group. No obvious effects on cell viability were induced in the Au@Bi_2S_3-PVP NB group. The cell inhibition rate accelerated with increasing concentration in both the Au@Bi_2S_3-PVP + NIR and Au@Bi_2S_3-PVP/DOX + NIR groups, thus suggesting that the Au@Bi_2S_3-PVP NBs were able to effectively kill HepG2 cells by acting as a PT agent under the NIR laser irradiation. Furthermore, the DOX released from the Au@Bi_2S_3-PVP/DOX nanocomposites showed dose-dependent cytotoxicity and induction of cell death; therefore, Au@Bi_2S_3-PVP NBs could further serve as nanocarriers of anticancer drugs for chemotherapy. More importantly, a markedly enhanced inhibition effect was found in the Au@Bi_2S_3-PVP/DOX + NIR group compared with both the free DOX and Au@Bi_2S_3-PVP + NIR groups at an equivalent concentration. Therefore, the prepared Au@Bi_2S_3-PVP NBs not only showed preferable PT ablation of HepG2 cells and effective DOX delivery for cancer chemotherapy, but also exhibited a significantly enhanced therapeutic efficiency of cancer as a result of the combination of PTT with chemotherapy, as compared with the individual *in vitro* treatment. All the results indicated that Au@Bi_2S_3-PVP/DOX may be a powerful agent with promise for applications in combined chemo/PT therapy for liver cancer.

3.8. Investigations of in vitro migration and colony formation

The cell scratch method is often used to assess cell migration ability by incubation of cells with drugs. The growth and forward movement of the surrounding cells to the central scratch area indicate the presence of cell migration. Fig. 7A and B shows the clear treatment time-dependent migration of the HepG2 cells to the scratch area in both control (PBS) and Au@Bi_2S_3-PVP NB treated groups; the cell migration rate was maintained at over 57% and 42% for HepG2 cells in each group after treatment for more than 24 h (Fig. 7B). However, after the 24 h treatment with Au@Bi_2S_3-PVP/DOX, the migration of the HepG2 cells to scratch area was not obviously observed. These results revealed that the Au@Bi_2S_3-PVP/DOX nanocomposites were highly active in inhibiting the migration of HepG2 cells, and would probably weaken *in vivo* tumor migration. As more free Au@Bi_2S_3-PVP/DOX nanocomposites became available to enter cancer cells as a result of the improved solubility, the activity of HepG2 cells were significantly inhibited, thus causing weak migration of HepG2 cells to the scratch area after treatment.

The proliferation ability of single HepG2 cells is usually evaluated *via* colony formation assays. As described for the *in vitro* cytotoxicity assays, Au@Bi_2S_3-PVP/DOX + NIR exhibited a favorable inhibition rate against the growth of HepG2 cells, and thus was chosen as the optimal concentration throughout the colony formation assays. The same concentration was applied to DOX, Au@Bi_2S_3-PVP NBs, Au@Bi_2S_3-PVP/DOX and Au@Bi_2S_3-PVP + NIR for comparison. As shown in Fig. 7C and D, the colony formation rate of HepG2 was higher than 50% in the DOX-treated group, as compared with than in the control group. Without DOX, a high colony formation rate (almost 100%) was observed in the Au@Bi_2S_3-PVP NBs group, a result indicative of the poor inhibition in the colony formation of HepG2 cancer cells. In contrast, the colony formation (less than 10%) was dramatically inhibited after Au@Bi_2S_3-PVP/DOX + NIR was applied, thus verifying the excellent anti-cell-proliferation activity of Au@Bi_2S_3-PVP/DOX + NIR toward HepG2 cancer cells. The outstanding bioavailability and solubility of Au@Bi_2S_3-PVP/DOX appears to strongly contribute to the excellent anti-proliferation capability.

3.9. In vitro fluorescence staining

Using fluorescence microscopy, we further examined the influence of different formulations on the intracellular localization of DOX and cell apoptosis (Fig. 8). After propidium iodide (PI) staining, the cells treated with free DOX showed red fluorescence, thus indicating fast diffusion and internalization of DOX. After incubation with DOX for 24 h, most of the DOX was clearly visible in cellular nuclei, Au@Bi_2S_3-PVP/DOX and Au@Bi_2S_3-PVP/DOX + NIR. As shown in Fig. 8A and B, Au@Bi_2S_3-PVP/DOX efficiently delivered DOX into living HepG2 cells, thus suggesting that the drug release profile within cancer cells was dependent on the time and pH. Additionally, cell division clearly occurred in both the control and Au@Bi_2S_3-PVP groups (Hoechst staining), whereas cell division was effectively controlled in the DOX, Au@Bi_2S_3-PVP/DOX, Au@Bi_2S_3-PVP + NIR and Au@Bi_2S_3-PVP/DOX + NIR groups. In comparison, Au@Bi_2S_3-PVP/DOX + NIR induced the most efficient apoptosis among these six groups.

To further visually demonstrate the synergistic killing effect on cancer cells after various treatments, we stained both living and dead HepG2 cells with calcein AM (green) and PI (red), respectively. As shown in Fig. 8C, bright green fluorescence without a red signal was observed for HepG2 cells after exposure to the 808 NIR laser only, and the red signal was clearly strengthened after the HepG2 cells were treated with Au@Bi_2S_3-PVP/DOX. However, the combination of Au@Bi_2S_3-PVP/DOX with laser irradiation led to remarkable cell death, wherein strong red fluorescence signals were observed in HepG2 cells treated with both Au@Bi_2S_3-PVP/DOX and the NIR laser for 12 h, thus indicating that cell apoptosis was intensively induced after the combined treatment. These results further confirmed that the Au@Bi_2S_3-PVP/DOX nanocomposites may serve as a powerful and promising agent for synergistic chemo/PT therapy of cancer.

3.10. PA and CT imaging of Au@Bi_2S_3-PVP NBs

As mentioned above, Au@Bi_2S_3-PVP NBs performed efficient PT

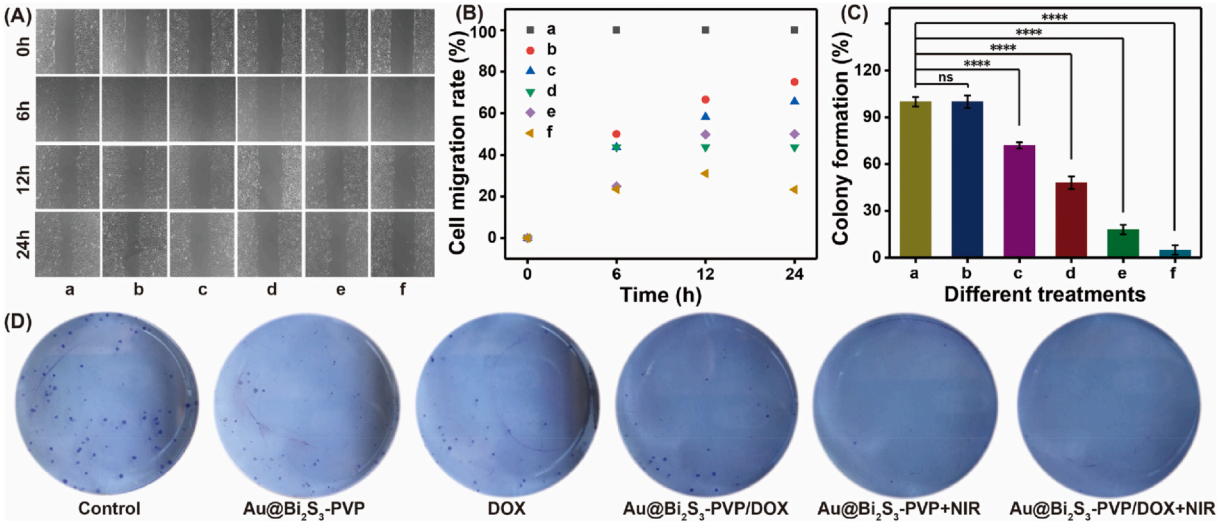

Fig. 7. The effects of a) control, b) Au@Bi_2S_3-PVP NBs, c) free DOX, d) Au@Bi_2S_3-PVP/DOX, e) Au@Bi_2S_3-PVP + NIR and f) Au@Bi_2S_3-PVP/DOX + NIR on A) HepG2 cell motility conducted through cell migration evaluation and D) single HepG2 cell proliferation conducted through colony formation evaluation; the corresponding changes in B) migration rate and C) colony formation rate, with control as comparison. Data are provided as the mean ± SD of five individual experiments (*p < 0.03, **p < 0.002, ***p < 0.0002 and ****p < 0.0001).

conversion during the PTT of liver cancer under irradiation by an 808 nm NIR laser. The NIR adsorption peak resulted from the localized SPR of Au@Bi_2S_3 and was located in the NIR-I window (680–970 nm) favorable for bioimaging applications such as PA imaging [76,77]. As shown in Fig. 9A and B, the PA absorbance of the aqueous solutions containing Au@Bi_2S_3-PVP NBs was linearly dependent on the concentration of Au@Bi_2S_3-PVP NBs ranging from 0 to 2.0 mg mL^{-1}, as expected. Given the remarkable *in vitro* PA imaging response and excellent biocompatibility of Au@Bi_2S_3-PVP NBs, *in vivo* PA imaging using Au@Bi_2S_3-PVP NBs as contrast agents was further performed with an excitation wavelength from 680 to 970 nm. Before and after the TV or IT injection of Au@Bi_2S_3-PVP NBs, the PA images of the mouse tumor were recorded (Fig. 9C). The PA signal intensity of the tumor site without injection of Au@Bi_2S_3-PVP NBs was too low to discriminate the tumor tissue from the surrounding normal tissue because of the weak intrinsic absorption of tumor tissue. However, after the administration of Au@Bi_2S_3-PVP NBs through TV injection, the PA signal in the tumor region was significantly enhanced, thus allowing the tumor profile to be distinguished as a result of the gradual accumulation of the Au@Bi_2S_3-PVP NBs inside tumors, probably because of the enhanced permeability and retention (EPR) effect [76,77]. Moreover, the PA signal intensity visually increased with prolonged retention times (2 h, 4 h and 6 h) in circulation, as shown in Fig. 9C, thus indicating the time-dependent accumulation of Au@Bi_2S_3-PVP NBs at the tumor site. Importantly, the intensity of the PA signal at tumor sites was comparable for TV and IV injections of Au@Bi_2S_3-PVP NBs, thus further verifying the effective accumulation of Au@Bi_2S_3-PVP NBs at the tumor site. This finding should be highly important for PA imaging guided therapy for tumors.

Bi's high atomic number endows it with extraordinary X-ray attenuation ability, thus prompting the application of biocompatible Au@Bi_2S_3-PVP NBs in CT imaging as a contrast enhancing agent [78,79]. In the medical field, CT is a popular imaging tool for diagnosis because it can deeply penetrate tissues and has high resolution. Here, with a clinical scanner, the CT performance of the Au@Bi_2S_3-PVP NBs was evaluated in nude tumor-bearing mice. A total of 100 μL of Au@Bi_2S_3-PVP NBs at a concentration of 500 μg mL^{-1} was injected into anesthetized mice *via* TV injection and IT injection, and PBS was used as a control; the CT images are shown in Fig. 9D. After being injected with

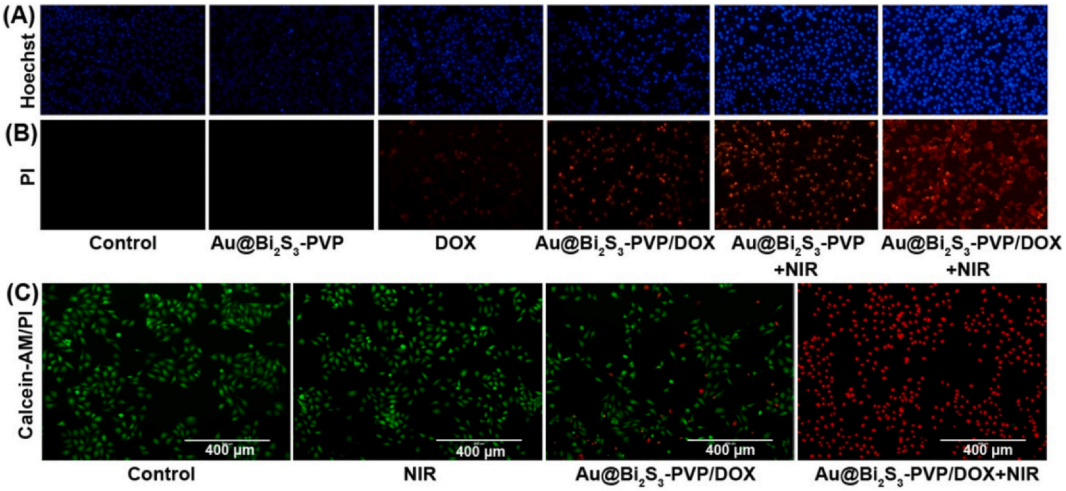

Fig. 8. A) Hoechst and B) PI staining of different treatments for 24 h. 1) control, 2) Au@Bi_2S_3-PVP NBs, 3) DOX, 4) Au@Bi_2S_3-PVP/DOX, 5) Au@Bi_2S_3-PVP + NIR, 6) Au@Bi_2S_3-PVP/DOX + NIR; C) Calcein-AM/PI staining of different treatments for 12 h. 1) control, 2) NIR, 3) Au@Bi_2S_3-PVP/DOX, 4) Au@Bi_2S_3-PVP/DOX + NIR. Scale bar: 400 μm.

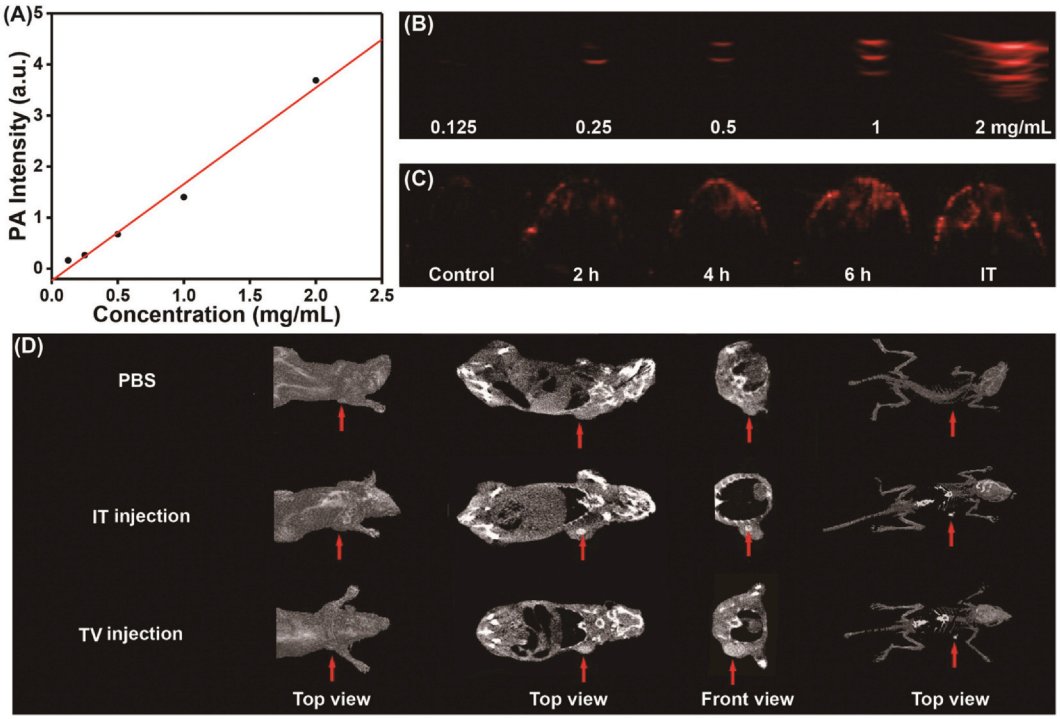

Fig. 9. A) Quantitative measurement of PA signals and B) PA images of Au@Bi_2S_3-PVP NB solutions at various concentrations; C) *in vivo* PA images of tumor sites in tumor model mice before and after TV and IT injection of Au@Bi_2S_3-PVP NB solution; D) *in vivo* CT imaging of tumors. The tumor site is indicated with a red arrow in top and front view 1 h after injection.

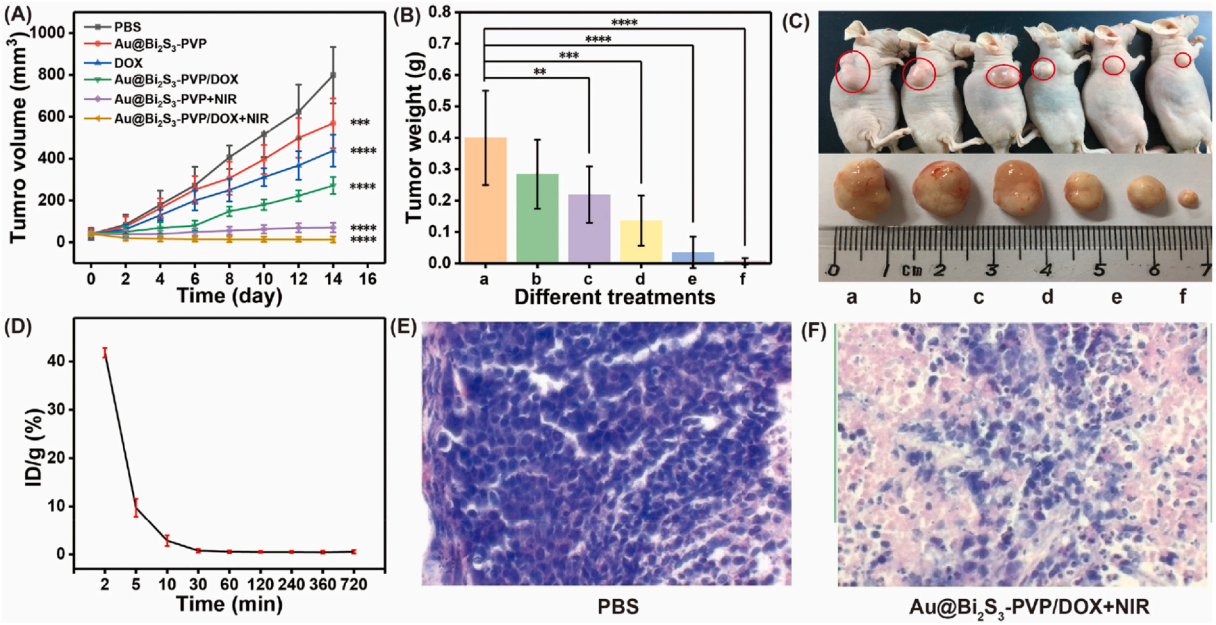

Fig. 10. (A) Tumor volume, (B) tumor weight and (C) tumor images after treatment with a) PBS, b) Au@Bi_2S_3-PVP NBs, c) free DOX, d) Au@Bi_2S_3-PVP/DOX, e) Au@Bi_2S_3-PVP + NIR and f) Au@Bi_2S_3-PVP/DOX + NIR through TV injection; D) Pharmacokinetic profiles of Au@Bi_2S_3-PVP/DOX in the plasma in a HepG2 tumor-bearing BALB/c nude mouse model administered *via* TV injection. Hematoxylin & eosin (HE) staining of tumor tissues after treatment with (E) PBS and (F) Au@Bi_2S_3-PVP/DOX + NIR. Data are provided as the mean ± SD of five individual experiments (*p < 0.03, **p < 0.002, ***p < 0.0002 and ****p < 0.0001).

Au@Bi_2S_3-PVP NBs, the tumor sites showed clear high image contrast, with the tumor region becoming much brighter. The clear CT contract enhancement of the liver and spleen suggested that Au@Bi_2S_3-PVP NBs accumulated *via* reticuloendothelial system (RES) absorption and were further metabolized and removed through the liver and spleen [80,81]. Moreover, compared with the previously reported Bi-BSA NRs [59], Au@Bi_2S_3-PVP NBs displayed more obvious CT contract in tumor regions, thus enabling monitoring of the degree of Au@Bi_2S_3-PVP NB accumulation in the tumors for effective PTT and identification of the size and location of tumors too small to be visible. In addition, the injection mode (IT or TV) influenced the contract intensity of the tumor region. IT injection was more visible than TV injection, owing to the longer blood circulation of TV injection, which probably weakened the accumulation of Au@Bi_2S_3-PVP NBs in the tumor region. Furthermore,

the CT performance of Au@Bi_2S_3-PVP NBs was comparable to or even better than that of quantum dots (~16 nm [66], 2–6 nm [82]), carbon dots (~4.2 nm [83], ~20 nm [84]), Au/Ag/Cu nanoclusters (~73.8 nm [85], 50 nm [86], 3 nm [87]), upconversion nanoparticles (UCNPs, ~14 nm [88], ~52.8 nm [89]) and several other nanoparticles with particle sizes above 100 nm, such as Bi_2S_3-PEG Nus [57]. These results indicated the great potential of Au@Bi_2S_3-PVP NBs to perform CT imaging of tumors.

3.11. In vivo antitumor effects

Comparative studies of effectiveness in tumor inhibition were conducted to investigate *in vivo* therapeutic efficacy of Au@Bi_2S_3-PVP NBs. Thirty female nude mice with the HepG2 human liver cancer cell model were randomly distributed into six groups: control, Au@Bi_2S_3-PVP NBs, DOX, Au@Bi_2S_3-PVP/DOX, Au@Bi_2S_3-PVP + NIR and Au@Bi_2S_3-PVP/DOX + NIR. Here, the DOX dosage was equivalent between the Au@Bi_2S_3-PVP/DOX + NIR group and other DOX groups. The tumors in both Au@Bi_2S_3-PVP + NIR and Au@Bi_2S_3-PVP/DOX + NIR groups were irradiated *via* an 808 nm laser for 3 min under a power density of 1.45 W/cm^2. No irradiation was applied in the three groups of PBS (control), Au@Bi_2S_3-PVP NBs and DOX. During the 14-day therapy, no mice died. The mice were killed on the 15th day, and tumors were excised and weighed (Fig. 10). The tumor volume was monitored every other day in each group (Fig. 10A). Of note, at the beginning of treatment (day 0), the mice in each group had homogeneous tumor volumes. After the termination of treatment, the mean tumor weights in each group were recorded (Fig. 10B). Compared with the control, the Au@Bi_2S_3-PVP + NIR group exhibited enhanced inhibition activity and a smaller mean tumor weight of 0.035 ± 0.05 g (control: 0.400 ± 0.150 g), thus demonstrating that Au@Bi_2S_3-PVP NBs effectively inhibited the tumor growth under the NIR laser irradiation. However, after treatment with the Au@Bi_2S_3-PVP/DOX + NIR, the most significantly enhanced antitumor activity among the six groups was obtained, and the mean tumor volume on day 4 had decreased to almost 0.007 mm^3, a value significantly smaller than that of any other group, as seen from the photographs of the tumor-bearing mice and the exfoliated tumors in Fig. 10C. The injection was planned on day 0 for treatment, and a marked therapeutic effect was observed in the Au@Bi_2S_3-PVP/DOX group receiving the same DOX dosage as the free DOX group, thus indicating the excellent drug delivery efficiency of Au@Bi_2S_3-PVP NBs. After a 6-day treatment, the tumor volume increased markedly faster than that at 6 days before, thus suggesting that 6 or 7 days might achieve the ideal treatment efficiency for Au@Bi_2S_3-PVP/DOX. That is, Au@Bi_2S_3-PVP/DOX required 6 or 7 days to slowly release DOX. These results indicated that Au@Bi_2S_3-PVP NBs have substantial PT and chemotherapeutic effects in cancer treatment. Furthermore, the long *in vivo* blood circulation of Au@Bi_2S_3-PVP/DOX significantly enhanced the therapeutic efficacy toward tumors. Accordingly, the pharmacokinetic behavior of Au@Bi_2S_3-PVP/DOX was studied by monitoring the concentrations of Au in the plasma in a HepG2 tumor-bearing BALB/c nude mouse model administered Au@Bi_2S_3-PVP/DOX *via* TV injection. The pharmacokinetic profiles in Fig. 10D clearly displayed a long blood circulation time of Au@Bi_2S_3-PVP/DOX within 12 h—a duration comparable to those of several other reported materials, thus further supporting the excellent therapeutic effects of Au@Bi_2S_3-PVP/DOX in tumor treatment [90,91].

The Au@Bi_2S_3-PVP NBs may function as a PT agent to ablate cancer cells *in vitro* and *in vivo*. After injection with Au@Bi_2S_3-PVP NBs and a 3-min irradiation, the HE staining was used for histological examination of the tumors, in which degenerative changes of coagulative necrosis were clearly observed in considerable tumor regions showing pyknosis, karyorrhexis and karyolysis, as compared with those injected with saline (Fig. 10E and F). Accordingly, the as-prepared Au@Bi_2S_3-PVP NBs can effectively destroy tumor cells *in vivo* by serving as a PT agent.

Immediately after the irradiation treatment, the tumor region became whitish, revealing the disruption of blood perfusion [92]. After 1 day of treatment, a black scar formed on the irradiated tumor area. Some scars partially fell off after the 10-day treatment. Tumors in the Au@Bi_2S_3-PVP + NIR group became smaller than those in the control group but were not completely inhibited after treatment, probably because of irradiation of small areas within the larger tumor area [93]. However, the mouse tumor volumes in the Au@Bi_2S_3-PVP/DOX + NIR group were much smaller than those in the Au@Bi_2S_3-PVP + NIR group, thus displaying enhanced antitumor activity of the Au@Bi_2S_3-PVP/DOX + NIR. The possible reasons for these results may be ascribed to i) a synergistic effect from the combination of chemotherapy with PTT and ii) the inhibition of tumor growth for a longer time as a result of sustained and slow DOX release from Au@Bi_2S_3-PVP/DOX after laser irradiation. Thus, Au@Bi_2S_3-PVP/DOX + NIR exhibited a markedly enhanced *in vivo* inhibition behavior over both Au@Bi_2S_3-PVP + NIR and free DOX, and ultimately led to effective PT/CT/PA-imaging bimodal guided chemo/PT synergistic cancer therapy.

3.12. Routine blood analysis, blood biochemistry and histopathological examination

To assess the potential *in vivo* toxicity of Au@Bi_2S_3-PVP NBs, we performed routine blood analysis and examined blood biochemistry and histopathology in the HepG2 tumor-bearing BALB/c nude mouse model injected IV with Au@Bi_2S_3-PVP/DOX. The healthy mice injected with PBS were used as the control group. Several routine blood indexes and hematological markers were analyzed immediately after the therapy, including white blood cells (WBCs), RBCs, erythrocyte distribution width (RDW), platelet mass distribution width (PMDW), platelets (PLT), platelet distribution width (PDW), platelet component distribution width (PCDW), mean platelet volume (MPV), mean platelet mass (MPM), mean platelet concentration (MPC), mean corpuscular volume (MCV), mean corpuscular hemoglobin concentration (MCHC), alanine aminotransferase (ALT), aspartate aminotransferase (AST), serum urea (UREA) and creatinine (CREA). As shown in Fig. 11A-P, the values of all selected blood indexes in the Au@Bi_2S_3-PVP/DOX-treated mice were in the normal biodistribution range. Furthermore, the histopathological examination of the tissues from major organs, such as the heart, liver, lung, spleen, and kidney, was conducted through standard histological techniques with HE staining. As shown in Fig. 11Q, neither noticeable apoptosis nor obvious pathological changes in major organs were observed in the Au@Bi_2S_3-PVP NBs, free DOX, Au@Bi_2S_3-PVP/DOX, Au@Bi_2S_3-PVP + NIR and Au@Bi_2S_3-PVP/DOX + NIR groups, thus collectively indicating the low *in vivo* systemic toxicity and good *in vivo* biocompatibility of the synthesized Au@Bi_2S_3-PVP NBs.

4. Conclusions

On the basis of Au@Bi_2S_3 core-shell NBs, we successfully developed a precision nanomedicine designed specifically for mutltimodal PT/PA/CT imaging-guided chemo/PT therapy for liver cancer. The as-prepared Au@Bi_2S_3-PVP NBs not only exhibited properties of strong NIR absorption, a high loading capacity for DOX, excellent biocompatibility and enhanced X-ray attenuation ability, but also provided a pH/NIR dual-responsive platform for synergistic chemo/PT cancer therapy. Importantly, the PCE of Au@Bi_2S_3 NBs was significantly enhanced by coating a Bi_2S_3 nanofilm on the surfaces Au NRs. These excellent properties of Au@Bi_2S_3-PVP NBs ensured the efficient PTT of HepG2 cancer cells and mutltimodal PT/PA/CT *in vivo* imaging for precise tumor destruction with the assistance of “visualization of satellite” and “precision of weapon”. The Au@Bi_2S_3-PVP NB based treatment inhibited both tumor growth in mice treated with NIR laser irradiation, indicating the effectiveness and importance of chemo/PT synergistic cancer therapy. Au@Bi_2S_3-PVP NBs, a powerful theranostic agent, had

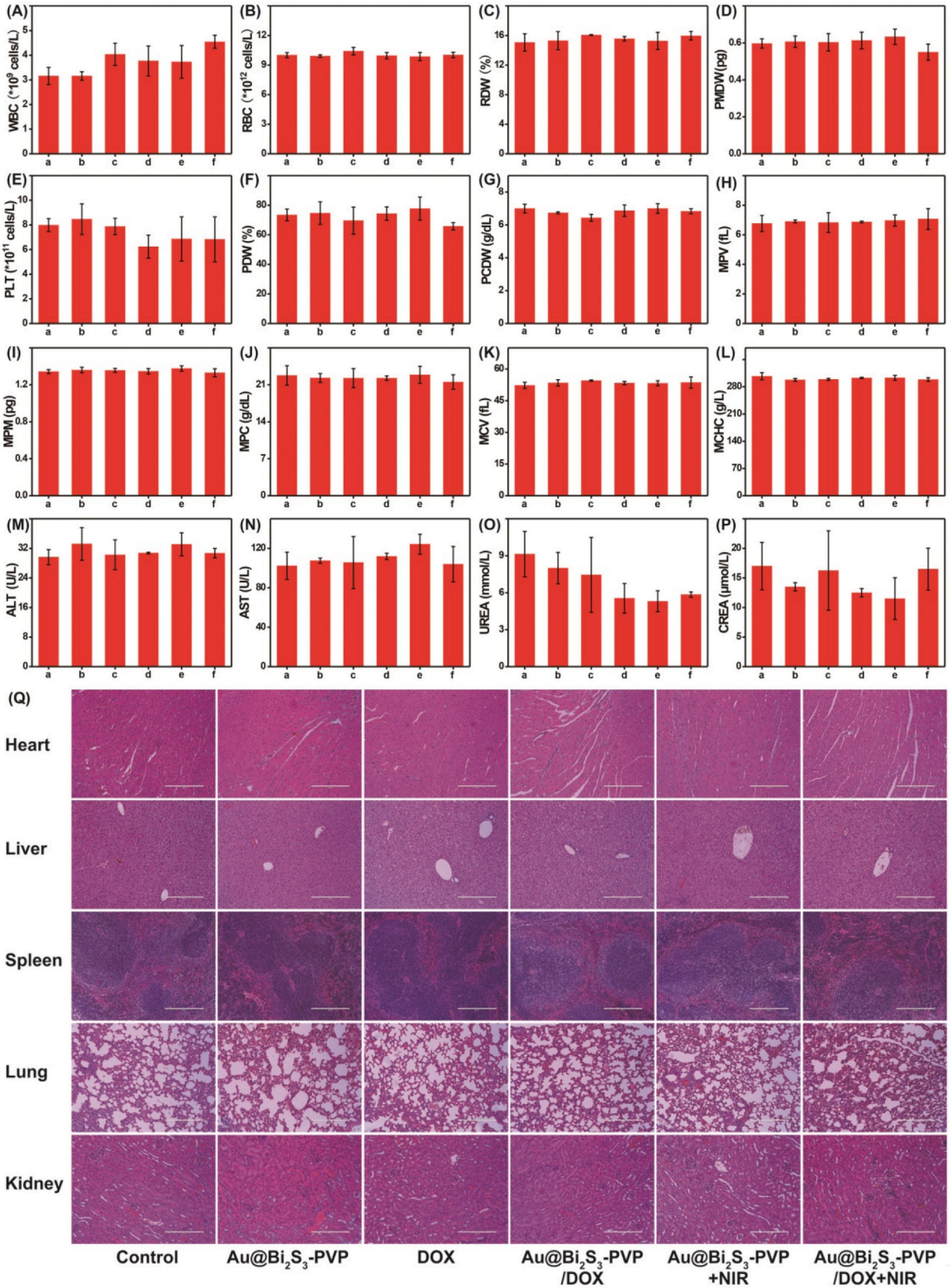

Fig. 11. (A–P) Routine blood tests and blood biochemistry: (A) WBC, (B) RBC, (C) RDW, (D) PMDM, (E) PLT, (F) PDW, (G) PCDW, (H) MPV, (I) MPM, (J) MPC, (K) MCV, (L) MCHC, (M) ALT, (N) AST, (O) UREA and (P) CREA; (Q) HE staining of tissues after treatment with PBS, Au@Bi_2S_3-PVP NBs, DOX, Au@Bi_2S_3-PVP/DOX, Au@Bi_2S_3-PVP + NIR and Au@Bi_2S_3-PVP/DOX + NIR. Data are provided as the mean ± SD of 3 individual experiments. Magnification: × 20.

no obvious influence on mouse body weight and did not cause pathological changes in major organ tissues. The discovery of Au@Bi_2S_3-PVP NBs provides new insights into combined chemo/PT therapy for cancer and expands the possibilities of nanocarriers as a multifunctional nanoplatform in such combined therapy.

Declaration of interest statement

There are no conflicts to declare in this manuscript.

CRediT authorship contribution statement

Ruizhuo Ouyang: Conceptualization. **Penghui Cao:** Conceptualization, Methodology, Investigation, Writing - original draft. **Pengpeng Jia:** Conceptualization, Methodology, Investigation, Writing - original draft. **Hui Wang:** Conceptualization, Methodology, Investigation, Writing - original draft. **Tianyu Zong:** Investigation, Validation. **Chenyu Dai:** Investigation, Validation. **Jie Yuan:** Resources, Data curation. **Yuhao Li:** Visualization. **Dong Sun:** Resources, Data curation. **Ning Guo:** Resources, Data curation. **Yuqing Miao:** Writing - review & editing, Supervision. **Shuang Zhou:** Writing - review & editing, Supervision, Funding acquisition.

Declaration of competing interest

There are no conflicts to declare.

Acknowledgements

This work was financially supported by the Natural Science Foundation of Shanghai (19ZR1434800, 19ZR1461900), the National Natural Science Foundation of China (21305090) and the Fundamental Research Funds for the Central Universities (to Shuang Zhou). The authors greatly appreciated these supports. We thank Ms. Ling Cha from the Department Laboratory Diagnostics of Changhai Hospital (Shanghai, China) for providing the blood samples.

References

[1] X. Wang, S. Gao, Z. Qin, R. Tian, G. Wang, X. Zhang, L. Zhu, X. Chen, Evans blue derivative-functionalized gold nanorods for photothermal therapy-enhanced tumor chemotherapy, ACS Appl. Mater. Interfaces 10 (2018) 15140–15149.
[2] M.L. Chen, W.Q. Zhang, K. Yuan, M.X. Bo, B. Chen, L. Li, Q.J. Ma, L. Zhu, S. Gao, Preclinical Evaluation and Monitoring of the Therapeutic Response of a Dual Targeted Hyaluronic Acid Nanodrug, Contrast Media Mol. I., 2017 4972701.
[3] M. Zhang, X. Chen, L. Zhang, L. Li, Z.-M. Su, C. Wang, Spadix-bract structured nanobowls for bimodal imaging-guided multidrug chemo-photothermal synergistic therapy, Chem. Mater. 30 (2018) 3722–3733.
[4] C.M. Jimenez, D. Aggad, J.G. Croissant, K. Tresfield, D. Laurencin, D. Berthomieu, N. Cubedo, M. Rossel, S. Alsaiari, D.H. Anjum, R. Sougrat, M.A. Roldan-Gutierrez, S. Richeter, E. Oliviero, L. Raehm, C. Charnay, X. Cattoen, S. Clement, M.W.C. Man, M. Maynadier, V. Chaleix, V. Sol, M. Garcia, M. Gary-Bobo, N.M. Khashab, N. Bettache, J.O. Durand, Porous porphyrin-based organosilica nanoparticles for NIR two-photon photodynamic therapy and gene delivery in zebrafish, Adv. Funct. Mater. 28 (2018) 1800235.
[5] D. Zhang, Z. Cai, N. Liao, S. Lan, M. Wu, H. Sun, Z. Wei, J. Li, X. Liu, pH/hypoxia programmable triggered cancer photo-chemotherapy based on a semiconducting polymer dot hybridized mesoporous silica framework, Chem. Sci. 9 (2018) 7390–7399.
[6] C. Wang, C. Xu, L. Xu, C. Sun, D. Yang, J. Xu, F. He, S. Gai, P. Yang, A novel core-shell structured upconversion nanorod as multimodal bioimaging and photothermal ablation agent for cancer theranostics, J. Math. Chem. B 6 (17) (2018) 2597–2607.
[7] Y.H. Li, Y. Sun, T.Y. Cao, Q.Q. Su, Z.L. Li, M.X. Huang, R.Z. Ouyang, H.Z. Chang, S.P. Zhang, Y.Q. Miao, A cation-exchange controlled core-shell MnS@Bi2S3 theranostic platform for multimodal imaging guided radiation therapy with hyperthermia boost, Nanoscale 9 (2017) 14364–14375.
[8] J. Zhu, J. Wang, X. Wang, J. Zhu, Y. Yang, J. Tian, W. Cui, C. Ge, Y. Li, Y. Pan, H. Gu, Facile synthesis of magnetic core–shell nanocomposites for MRI and CT bimodal imaging, J. Mater. Chem. B 3 (2015) 6905–6910.
[9] S.Y. Ding, J. Yi, J.F. Li, B. Ren, D.Y. Wu, R. Panneerselvam, Z.Q. Tian, Nanostructure-based plasmon-enhanced Raman spectroscopy for surface analysis of materials, Nat. Rev. Mater. 1 (2016) 16021.
[10] X. Yang, M.X. Yang, B. Pang, M. Vara, Y.N. Xia, Gold nanomaterials at work in biomedicine, Chem. Rev. 115 (2015) 10410–10488.
[11] N.N. Zhao, J. Li, Y.Q. Zhou, Y. Hu, R.R. Wang, Z.X. Ji, F.S. Liu, F.J. Xu, Hierarchical nanohybrids of gold nanorods and PGMA-based polycations for multifunctional theranostics, Adv. Funct. Mater. 26 (2016) 5848–5861.
[12] B.K. Jung, Y.K. Lee, J. Hong, H. Ghandehari, C.O. Yun, Mild hyperthermia induced by gold nanorod-mediated plasmonic photothermal therapy enhances transduction and replication of oncolytic adenoviral gene delivery, ACS Nano 10 (2016) 10533–10543.
[13] W.T. Shang, C.T. Zeng, Y. Du, H. Hui, X. Liang, C.W. Chi, K. Wang, Z.L. Wang, J. Tian, Core-shell gold Nanorod@Metal-organic framework nanoprobes for multimodality diagnosis of glioma, Adv. Mater. 29 (2017) 1604381.
[14] J. Wang, C.H. Zhu, J. Han, N. Han, J.Q. Xi, L. Fan, R. Guo, Controllable synthesis of gold nanorod/conducting polymer core/shell hybrids toward in vitro and in vivo near-infrared photothermal therapy, ACS Appl. Mater. Interfaces 10 (2018) 12323–12330.
[15] X.W. Wang, W. Gao, H.H. Fan, D. Ding, X.F. Lai, Y.X. Zou, L. Chen, Z. Chen, W.H. Tan, Simultaneous tracking of drug molecules and carriers using aptamer-functionalized fluorescent superstable gold nanorod-carbon nanocapsules during thermo-chemotherapy, Nanoscale 8 (2016) 7942–7948.
[16] J.K. Rad, A.R. Mahdavian, S. Khoei, S. Shirvalilou, Enhanced photogeneration of reactive oxygen species and targeted photothermal therapy of C6 glioma brain cancer cells by folate-conjugated gold-photoactive polymer nanoparticles, ACS Appl. Mater. Interfaces 10 (2018) 19483–19493.
[17] L. Qin, G.M. Zeng, C. Lai, D.L. Huang, P.A. Xu, C. Zhang, M. Cheng, X.G. Liu, S.Y. Liu, B.S. Li, H. Yi, Gold rush" in modern science: fabrication strategies and typical advanced applications of gold nanoparticles in sensing, Coord. Chem. Rev. 359 (2018) 1–31.
[18] C.L. Du, A.H. Wang, J.B. Fei, J. Zhao, J.B. Li, Polypyrrole-stabilized gold nanorods with enhanced photothermal effect towards two-photon photothermal therapy, J. Math. Chem. B 3 (2015) 4539–4545.
[19] C.B. Leng, X. Zhang, F.X. Xu, Y. Yuan, H. Pei, Z.H. Sun, L. Li, Z.H. Bao, Engineering gold nanorod-copper sulfide heterostructures with enhanced photothermal conversion efficiency and photostability, Small 14 (2018) 1703077.
[20] Y.T. Li, J. Jin, D.W. Wang, J.W. Lv, K. Hou, Y.L. Liu, C.Y. Chen, Z.Y. Tang, Coordination-responsive drug release inside gold nanorod@metal-organic framework core-shell nanostructures for near-infrared-induced synergistic chemo-photothermal therapy, Nano Res 11 (2018) 3294–3305.
[21] J.Y. Zeng, M.K. Zhang, M.Y. Peng, D. Gong, X.Z. Zhang, Porphyrinic metal-organic frameworks coated gold nanorods as a versatile nanoplatform for combined photodynamic/photothermal/chemotherapy of tumor, Adv. Funct. Mater. 28 (2018) 1705451.
[22] Z. Xiao, C. Xu, X. Jiang, W. Zhang, Y. Peng, R. Zou, X. Huang, Q. Liu, Z. Qin, J. Hu, Hydrophilic bismuth sulfur nanoflower superstructures with an improved photothermal efficiency for ablation of cancer cells, Nano Res 9 (2016) 1934–1947.
[23] G.G. Briand, N. Burford, Bismuth compounds and preparations with biological or medicinal relevance, Chem. Rev. 99 (1999) 2601–2657.
[24] E.R.T. Tiekink, Antimony and bismuth compounds in oncology, Crit. Rev. Oncol.-Hematol. 42 (2002) 217–224.
[25] W. Li, L. Jin, N.Y. Zhu, X.M. Hou, F. Deng, H.Z. Sun, Structure of colloidal bismuth subcitrate (CBS) in dilute HCl: unique assembly of bismuth citrate dinuclear units ([Bi(cit)(2)Bi](2-)), J. Am. Chem. Soc. 125 (2003) 12408–12409.
[26] P.C. Andrews, G.B. Deacon, C.M. Forsyth, P.C. Junk, I. Kumar, M. Maguire, Towards a structural understanding of the anti-ulcer and anti-gastritis drug bismuth subsalicylate, Angew. Chem. Int. Ed. 45 (2006) 5638–5642.
[27] K.D. Mjos, C. Orvig, Metallodrugs in medicinal inorganic chemistry, Chem. Rev. 114 (2014) 4540–4563.
[28] R.Z. Ouyang, Y. Yang, X. Tong, K. Feng, Y.Q. Yang, H.H. Tao, X.S. Zhang, T.Y. Zong, P.H. Cao, F. Xiong, N. Guo, Y.H. Li, Y.Q. Miao, S. Zhou, Potent anticancer activity of a new bismuth (III) complex against human lung cancer cells, J. Inorg. Biochem. 168 (2017) 18–26.
[29] O. Rabin, J.M. Perez, J. Grimm, G. Wojtkiewicz, R. Weissleder, An X-ray computed tomography imaging agent based on long-circulating bismuth sulphide nanoparticles, Nat. Mater. 5 (2006) 118–122.
[30] X.D. Zhang, J. Chen, Y. Min, G.B. Park, X. Shen, S.S. Song, Y.M. Sun, H. Wang, W. Long, J.P. Xie, K. Gao, L.F. Zhang, S.J. Fan, F.Y. Fan, U. Jeong, Metabolizable Bi 2 Se 3 nanoplates: biodistribution, toxicity, and uses for cancer radiation therapy and imaging, Adv. Funct. Mater. 24 (2014) 1718–1729.
[31] X.P. Zheng, J.X. Shi, Y. Bu, G. Tian, X. Zhang, W.Y. Yin, B.F. Gao, Z.Y. Yang, Z.B. Hu, X.F. Liu, L. Yan, Z.J. Gu, Y.L. Zhao, Silica-coated bismuth sulfide nanorods as multimodal contrast agents for a non-invasive visualization of the gastrointestinal tract, Nanoscale 7 (2015) 12581–12591.
[32] Y. Cheng, Y. Chang, Y. Feng, H. Jian, Z. Tang, H. Zhang, Deep-level defect enhanced photothermal performance of bismuth sulfide-gold heterojunction nanorods for photothermal therapy of cancer guided by computed tomography imaging, Angew. Chem. Int. Ed. 57 (2018) 246–251.
[33] T.T. Zhang, C.H. Xu, W. Zhao, Y. Gu, X.L. Li, J.J. Xu, H.Y. Chen, A redox-activated theranostic nanoagent: toward multi-mode imaging guided chemo-photothermal therapy, Chem. Sci. 9 (2018) 6749–6757.
[34] X.C. Ye, L.H. Jin, H. Caglayan, J. Chen, G.Z. Xing, C. Zheng, V. Doan-Nguyen, Y.J. Kang, N. Engheta, C.R. Kagan, C.B. Murray, Improved size tumable synthesis of monodisperse gold nanorods through the use of aromatic additives, ACS Nano 6 (2012) 2804–2817.
[35] G.S. Song, C. Liang, H. Gong, M.F. Li, X.C. Zheng, L. Cheng, K. Yang, X.Q. Jiang, Z. Liu, Core-shell MnSe@Bi2Se3 fabricated via a cation exchange method as novel nanotheranostics for multimodal imaging and synergistic thermoradiotherapy, Adv. Mater. 27 (2015) 6110–6117.

[36] G.S. Song, C. Liang, X. Yi, Q. Zhao, L. Cheng, K. Yang, Z.A. Liu, Perfluorocarbon-loaded hollow Bi2Se3 nanoparticles for timely supply of oxygen under near-infrared light to enhance the radiotherapy of cancer, Adv. Mater. 28 (2016) 2716–2723.
[37] N.R. Jana, L. Gearheart, C.J. Murphy, Wet chemical synthesis of high aspect ratio cylindrical gold nanorods, J. Phys. Chem. B 105 (2001) 4065–4067.
[38] B. N, M.A. Elsayed, Preparation and growth mechanism of gold nanorods (NRs) using seed-mediated growth method, Chem. Mater. 15 (2003) 1957–1962.
[39] T.K. Sau, C.J. Murphy, Seeded high yield synthesis of short Au nanorods in aqueous solution, Langmuir 20 (2004) 6414–6420.
[40] T.K. Sau, C.J. Murphy, Role of ions in the colloidal synthesis of gold nanowires, Philos. Mag. A 87 (2007) 2143–2158.
[41] X. Ye, L. Jin, H. Caglayan, J. Chen, G. Xing, C. Zheng, V. Doan-Nguyen, Y. Kang, N. Engheta, C.R. Kagan, C.B. Murray, Improved size-tunable synthesis of monodisperse gold nanorods through the use of aromatic additives, ACS Nano 6 (2012) 2804–2817.
[42] X. Ye, C. Zheng, J. Chen, Y. Gao, C.B. Murray, Using binary surfactant mixtures to simultaneously improve the dimensional tunability and monodispersity in the seeded growth of gold nanorods, Nano Lett. 13 (2013) 765–771.
[43] C.B. Roxlo, B. Abeles, C.R. Wronski, G.D. Cody, T. Tiedje, Comment on the optical absorption edge in a-Si:H, Solid State Commun. 47 (1983) 985–987.
[44] L. Ma, S. Liang, X.-L. Liu, D.-J. Yang, L. Zhou, Q.-Q. Wang, Synthesis of dumbbell-like gold-metal sulfide core-shell nanorods with largely enhanced transverse plasmon resonance in visible region and efficiently improved photocatalytic activity, Adv. Funct. Mater. 25 (2015) 898–904.
[45] Y. Yang, S. Han, G. Zhou, L. Zhang, X. Li, C. Zou, S. Huang, Ascorbic-acid-assisted growth of high quality M@ZnO: a growth mechanism and kinetics study, Nanoscale 5 (2013) 11808–11819.
[46] J. Zhang, Y. Tang, K. Lee, M. Ouyang, Nonepitaxial growth of hybrid core-shell nanostructures with large lattice mismatches, Science 327 (2010) 1634–1638.
[47] Z. Sun, Z. Yang, J. Zhou, M.H. Yeung, W. Ni, H. Wu, J. Wang, A general approach to the synthesis of gold-metal sulfide core-shell and heterostructures, Angew. Chem. Int. Ed. 48 (2009) 2881–2885.
[48] S.B. Lakshmanan, X. Zou, M. Hossu, L. Ma, C. Yang, W. Chen, Local field enhanced Au/CuS nanocomposites as efficient photothermal transducer agents for cancer treatment, J. Biomed. Nanotechnol. 8 (2012) 883–890.
[49] Yuebin Li, Wei Liu, Qian Huang, Miao Huang, Li Chun, W. Chen, Copper sulfide nanoparticles for photothermal ablation of tumor cells, Nanomedicine 5 (2010) 1161–1171.
[50] Y.S. Lin, C.L. Haynes, Impacts of mesoporous silica nanoparticle size, pore ordering, and pore integrity on hemolytic activity, J. Am. Chem. Soc. 132 (2010) 4834–4842.
[51] Z. Zhang, L. Wang, J. Wang, X. Jiang, X. Li, Z. Hu, Y. Ji, X. Wu, C. Chen, Mesoporous silica-coated gold nanorods as a light-mediated multifunctional theranostic platform for cancer treatment, Adv. Mater. 24 (2012) 1418–1423.
[52] J.E. Wang, G.Y. Wang, Y. Sun, Y.F. Wang, Y. Yang, Y. Yuan, Y.L. Li, C.S. Liu, In Situ formation of pH-/thermo-sensitive nanohybrids via friendly-assembly of poly(N-vinylpyrrolidone) onto LAPONITE (R), RSC Adv. 6 (2016) 31816–31823.
[53] S.C. Park, Y. Yuan, K. Choi, S.O. Choi, J. Kim, Doxorubicin release controlled by induced phase separation and use of a Co-solvent, Materials 11 (2018) 681.
[54] G. Song, C. Li, J. Hu, R. Zou, K. Xu, L. Han, Q. Wang, J. Yang, Z. Chen, Z. Qin, K. Ruan, R. Hu, A simple transformation from silica core–shell–shell to yolk–shell nanostructures: a useful platform for effective cell imaging and drug delivery, J. Mater. Chem. 22 (2012) 17011–17018.
[55] H. Zhao, L. Li, J. Zhang, C. Zheng, K. Ding, H. Xiao, L. Wang, Z. Zhang, C-C chemokine ligand 2 (CCL2) recruits macrophage-membrane-camouflaged hollow bismuth selenide nanoparticles to facilitate photothermal sensitivity and inhibit lung metastasis of breast cancer, ACS Appl. Mater. Interfaces 10 (2018) 31124–31135.
[56] J. Liu, X. Zheng, L. Yan, L. Zhou, G. Tian, W. Yin, L. Wang, Y. Liu, Z. Hu, Z. Gu, C. Chen, Y. Zhao, Bismuth sulfide nanorods as a precision nanomedicine for in vivo multimodal imaging-guided photothermal therapy of tumor, ACS Nano 9 (2015) 696–707.
[57] Z.L. Li, Y. Hu, M.L. Chan, K.A. Howard, X.L. Fan, Y. Sun, F. Besenbacher, M. Yu, Highly porous PEGylated Bi2S3 nano-urchins as a versatile platform for in vivo triple-modal imaging, photothermal therapy and drug delivery, Nanoscale 8 (2016) 16005–16016.
[58] L.H. Li, Y. Lu, C.Y. Jiang, Y. Zhu, X.F. Yang, X.M. Hu, Z.F. Lin, Y. Zhang, M.Y. Peng, H. Xia, C.B. Mao, Actively targeted deep tissue imaging and photothermal-chemo therapy of breast cancer by antibody-functionalized drug-loaded X-ray-responsive bismuth Sulfide@Mesoporous silica core-shell nanoparticles, Adv. Funct. Mater. 28 (2018) 1704623.
[59] Z. Li, Y. Hu, Z. Miao, H. Xu, C. Li, Y. Zhao, Z. Li, M. Chang, Z. Ma, Y. Sun, F. Besenbacher, P. Huang, M. Yu, Dual-stimuli responsive bismuth nanoraspberries for multimodal imaging and combined cancer therapy, Nano Lett. 18 (2018) 6778–6788.
[60] Z. Li, Z. Li, L. Sun, B. Du, Y. Wang, G. Zhao, D. Yu, S. Yang, Y. Sun, M. Yu, Core–shell Bi2Se3@mSiO2-PEG as a multifunctional drug-delivery nanoplatform for synergistic thermo-chemotherapy with infrared thermal imaging of cancer cells, part. Part. Sys, Char 35 (2018) 1700337.
[61] L. Feng, D. Yang, S. Gai, F. He, G. Yang, P. Yang, J. Lin, Single bismuth tungstate nanosheets for simultaneous chemo-, photothermal, and photodynamic therapies mediated by near-infrared light, Chem. Eng. J. 351 (2018) 1147–1158.
[62] Y. Lu, L. Li, Z. Lin, M. Li, X. Hu, Y. Zhang, M. Peng, H. Xia, G. Han, Enhancing osteosacoma killing and CT imaging using ultrahigh drug loading and NIR-responsive bismuth Sulfide@Mesoporous silica nanoparticles, Adv. Healthc. Mater. 7 (2018) 1800602.
[63] Z. Gong, Y. Shi, H. Tan, L. Wang, Z. Gao, B. Lian, G. Wang, H. Sun, P. Sun, B. Zhou, J. Bai, Plasma amine oxidase-induced nanoparticle-to-nanofiber geometric transformation of an amphiphilic peptide for drug encapsulation and enhanced bactericidal activity, ACS Appl. Mater. Interfaces 12 (2020) 4323–4332.
[64] P.P. Lei, R. An, P. Zhang, S. Yao, S.Y. Song, L.L. Dong, X. Xu, K.M. Du, J. Feng, H.J. Zhang, Ultrafast synthesis of ultrasmall poly(vinylpyrrolidone)-protected bismuth nanodots as a multifunctional theranostic agent for in vivo dual-modal CT/Photothermal-Imaging-Guided photothermal therapy, Adv. Funct. Mater. 27 (2017) 10.
[65] Z. Li, J. Liu, Y. Hu, Z. Li, X. Fan, Y. Sun, F. Besenbacher, C. Chen, M. Yu, Biocompatible PEGylated bismuth nanocrystals: "All-in-one" theranostic agent with triple-modal imaging and efficient in vivo photothermal ablation of tumors, Biomaterials 141 (2017) 284–295.
[66] B. Wu, S.T. Lu, H. Yu, R.F. Liao, H. Li, B.V.L. Zafitatsimo, Y.S. Li, Y. Zhang, X.L. Zhu, H.G. Liu, H.B. Xu, S.W. Huang, Z. Cheng, Gadolinium-chelate functionalized bismuth nanotheranostic agent for in vivo MRI/CT/PAI imaging-guided photothermal cancer therapy, Biomaterials 159 (2018) 37–47.
[67] J. Liu, X.P. Zheng, L. Yan, L.J. Zhou, G. Tian, W.Y. Yin, L.M. Wang, Y. Liu, Z.B. Hu, Z.J. Gu, C.Y. Chen, Y.L. Zhao, Bismuth sulfide nanorods as a precision nanomedicine for in vivo multimodal imaging-guided photothermal therapy of tumor, ACS Nano 9 (2015) 696–707.
[68] S.S. Yang, Z.L. Li, Y.L. Wang, X.L. Fang, Z.H. Miao, Y. Hu, Z. Li, Y. Sun, F. Besenhacher, M. Yu, Multifunctional Bi@PPy-PEG core-shell nanohybrids for dual-modal imaging and photothermal therapy, ACS Appl. Mater. Interfaces 10 (2018) 1605–1615.
[69] Q.W. Tian, F.R. Jiang, R.J. Zou, Q. Liu, Z.G. Chen, M.F. Zhu, S.P. Yang, J.L. Wang, J.H. Wang, J.Q. Hu, Hydrophilic Cu9S5 nanocrystals: a photothermal agent with a 25.7% heat conversion efficiency for photothermal ablation of cancer cells in vivo, ACS Nano 5 (2011) 9761–9771.
[70] F. Scotognella, G. Della Valle, A.R.S. Kandada, D. Dorfs, M. Zavelani-Rossi, M. Conforti, K. Miszta, A. Comin, K. Korobcheyskaya, G. Lanzani, L. Manna, F. Tassone, Plasmon dynamics in colloidal Cu2-xSe nanocrystals, Nano Lett. 11 (2011) 4711–4717.
[71] C. Xu, F. Chen, H.F. Valdovinos, D. Jiang, S. Goel, B. Yu, H. Sun, T.E. Barnhart, J.J. Moon, W. Cai, Bacteria-like mesoporous silica-coated gold nanorods for positron emission tomography and photoacoustic imaging-guided chemo-photothermal combined therapy, Biomaterials 165 (2018) 56–65.
[72] N. Yu, Z.J. Wang, J.L. Zhang, Z.X. Liu, B. Zhu, J. Yu, M.F. Zhu, C. Peng, Z.G. Chen, Thiol-capped Bi nanoparticles as stable and all-in-one type theranostic nanoagents for tumor imaging and thermoradiotherapy, Biomaterials 161 (2018) 279–291.
[73] J. Kim, J. Kim, C. Jeong, W.J. Kim, Synergistic nanomedicine by combined gene and photothermal therapy, Adv. Drug Deliv. Rev. 98 (2016) 99–112.
[74] Z. Li, Y. Hu, M. Chang, K.A. Howard, X. Fan, Y. Sun, F. Besenbacher, M. Yu, Highly porous PEGylated Bi2S3 nano-urchins as a versatile platform for in vivo triple-modal imaging, photothermal therapy and drug delivery, Nanoscale 8 (2016) 16005–16016.
[75] B. Wu, S.T. Lu, H. Yu, R.F. Liao, H. Li, B.V. Lucie Zafitatsimo, Y.S. Li, Y. Zhang, X.L. Zhu, H.G. Liu, H.B. Xu, S.W. Huang, Z. Cheng, Gadolinium-chelate functionalized bismuth nanotheranostic agent for in vivo MRI/CT/PAI imaging-guided photothermal cancer therapy, Biomaterials 159 (2018) 37–47.
[76] L. Tan, J. Wan, W. Guo, C. Ou, T. Liu, C. Fu, Q. Zhang, X. Ren, X.J. Liang, J. Ren, L. Li, X. Meng, Renal-clearable quaternary chalcogenide nanocrystal for photoacoustic/magnetic resonance imaging guided tumor photothermal therapy, Biomaterials 159 (2018) 108–118.
[77] W. Yang, W. Guo, W. Le, G. Lv, F. Zhang, L. Shi, X. Wang, J. Wang, S. Wang, J. Chang, B. Zhang, Albumin-bioinspired Gd:CuS nanotheranostic agent for in vivo photoacoustic/magnetic resonance imaging-guided tumor-targeted photothermal therapy, ACS Nano 10 (2016) 10245–10257.
[78] C. Xu, G.A. Tung, S. Sun, Size and concentration effect of gold nanoparticles on X-ray attenuation as measured on computed tomography, Chem. Mater. 20 (2008) 4167–4169.
[79] D. Xi, S. Dong, X. Meng, Q. Lu, L. Meng, J. Ye, Gold nanoparticles as computerized tomography (CT) contrast agents, RSC Adv. 2 (2012) 12515–12524.
[80] M.F. Attia, N. Anton, M. Chiper, R. Akasov, H. Anton, N. Messaddeq, S. Fournel, A.S. Klymchenko, Y. Mély, T.F. Vandamme, Biodistribution of X-ray iodinated contrast agent in nano-emulsions is controlled by the chemical nature of the oily core, ACS Nano 8 (2014) 10537–10550.
[81] Z.L. Li, Y. Hu, K.A. Howard, T.T. Jiang, X.L. Fan, Z.H. Miao, Y. Sun, F. Besenbacher, M. Yu, Multifunctional bismuth selenide nanocomposites for antitumor thermo-chemotherapy and imaging, ACS Nano 10 (2016) 984–997.
[82] S.Y. Sung, Y.L. Su, W. Cheng, P.F. Hu, C.S. Chiang, W.T. Chen, S.H. Hu, Graphene quantum dots-mediated theranostic penetrative delivery of drug and photolytics in deep tumors by targeted biomimetic nanosponges, Nano Lett. 19 (2019) 69–81.
[83] Q. Jia, J. Ge, W. Liu, X. Zheng, S. Chen, Y. Wen, H. Zhang, P. Wang, A magneto-fluorescent carbon dot assembly as an acidic H_2O_2-driven oxygenerator to regulate tumor hypoxia for simultaneous bimodal imaging and enhanced photodynamic therapy, Adv. Mater. 30 (2018) e1706090.
[84] M. Lan, S. Zhao, Z. Zhang, L. Yan, L. Guo, G. Niu, J. Zhang, J. Zhao, H. Zhang, P. Wang, G. Zhu, C.-S. Lee, W. Zhang, Two-photon-excited near-infrared emissive carbon dots as multifunctional agents for fluorescence imaging and photothermal therapy, Nano Res 10 (2017) 3113–3123.
[85] S. Yu, R. Wen, H. Wang, Y. Zha, L. Qiu, B. Li, W. Xue, D. Ma, Chitosan-graft-Poly(l-lysine) dendron-assisted facile self-assembly of Au nanoclusters for enhanced X-ray computer tomography imaging and precise MMP-9 plasmid shRNA delivery, Chem. Mater. 31 (2019) 3992–4007.
[86] L. Zhang, R.P. Liang, S.J. Xiao, J.M. Bai, L.L. Zheng, L. Zhan, X.J. Zhao, J.D. Qiu, C.Z. Huang, DNA-templated Ag nanoclusters as fluorescent probes for sensing and intracellular imaging of hydroxyl radicals, Talanta 118 (2014) 339–347.

[87] F. Gao, P. Cai, W. Yang, J. Xue, L. Gao, R. Liu, Y. Wang, Y. Zhao, X. H, L. Zhao, G. Huang, F. Wu, Y. Zhao, Z. Chai, X. Gao, Ultrasmall [64 Cu]Cu nanoclusters for targeting orthotopic lung tumors using accurate positron emission tomography imaging, ACS Nano 9 (2015) 4976–4986.

[88] G. Chen, R. Jaskula-Sztul, C.R. Esquibel, I. Lou, Q. Zheng, A. Dammalapati, A. Harrison, K.W. Eliceiri, W. Tang, H. Chen, S. Gong, Neuroendocrine tumor-targeted upconversion nanoparticle-based micelles for simultaneous NIR-controlled combination chemotherapy and photodynamic therapy, and fluorescence imaging, Adv. Funct. Mater. 27 (2017) 1604671.

[89] C. Zhang, W.-H. Chen, L.-H. Liu, W.-X. Qiu, W.-Y. Yu, X.-Z. Zhang, An O_2 self-supplementing and reactive-oxygen-species-circulating amplified nanoplatform via H_2O/H_2O_2 splitting for tumor imaging and photodynamic therapy, Adv. Funct. Mater. 27 (2017) 1700626.

[90] J. Guo, Z. Yu, M. Das, L. Huang, Nano codelivery of oxaliplatin and folinic acid achieves synergistic chemo-immunotherapy with 5-fluorouracil for colorectal cancer and liver metastasis, ACS Nano 14 (2020) 5075–5089.

[91] L. Wang, C. Shi, X. Wang, D. Guo, T.M. Duncan, J. Luo, Zwitterionic Janus Dendrimer with distinct functional disparity for enhanced protein delivery, Biomaterials 215 (2019) 119233.

[92] J. You, R. Zhang, C. Xiong, M. Zhong, M. Melancon, S. Gupta, A.M. Nick, A.K. Sood, C. Li, Effective photothermal chemotherapy using doxorubicin-loaded gold nanospheres that target EphB4 receptors in tumors, Canc. Res. 72 (2012) 4777–4786.

[93] W. Zhang, Z. Guo, D. Huang, Z. Liu, X. Guo, H. Zhong, Synergistic effect of chemo-photothermal therapy using PEGylated graphene oxide, Biomaterials 32 (2011) 8555–8561.